166778

İSTANBUL TECHNICAL UNIVERSITY ★ INSTITUTE OF SCIENCE AND TECHNOLOGY

COMPUTATIONAL STUDY OF DYNAMIC STALL OVER PITCHING AIRFOILS

M.Sc. Thesis by
Erkan EVCAN, B.Sc.

(708021003)

Date of submission: 9 May 2005
Date of defence examination: 2 June 2005

Supervisor (Chairman): Assoc. Prof. Dr. Fırat Oğuz EDİS

Members of the Examining Committee: Prof. Dr. A. Rüstem ASLAN

Asst. Prof. Dr. Hayri ACAR

JUNE 2005

İSTANBUL TEKNİK ÜNİVERSİTESİ ★ FEN BİLİMLERİ ENSTİTÜSÜ

YUNUSLAMA YAPAN KANAT KESİTİNDE GÖRÜLEN DİNAMİK TUTUNMA KAYBININ HESAPLAMALI YÖNTEMLE İNCELENMESİ

YÜKSEK LİSANS TEZİ

Uçak Müh. Erkan EVCAN

(708021003)

Tezin Enstitüye Verildiği Tarih : 9 Mayıs 2005
Tezin Savunulduğu Tarih : 2 Haziran 2005

Tez Danışmanı : Doç. Dr. Fırat Oğuz EDİS

Diğer Jüri Üyeleri : Prof. Dr. A. Rüstem ASLAN

Yrd. Doç. Dr. Hayri ACAR

HAZİRAN 2005

FOREWORD

I would like to express my sincere appreciation to my advisor Assoc. Prof. Dr. Fırat Oğuz EDİS for his valuable guidance, contributions, helps and encouragements during the entire of this study.

I also extend thanks to my friends for their valuable encouragements.

Finally, I would like to take this opportunity to express my deepest love, appreciation, and gratitude to my family and Hacer YEGÜL for their continuous support and encouragement.

May, 2005 Erkan EVCAN

TABLE OF CONTENTS

ABBREVIATIONS

CFD	: Computational Fluid Dynamics
CFDRC	: CFD Research Corporation
NASA	: National Aeronautics and Space Administration
AGARD	: Advisory Group for Aerospace Research and Development
AIAA	: American Institute of Aeronautics and Astronautics
NACA	: National Advisory Committee for Aeronautics
ASME	: American Society of Mechanical Engineers
AoA	: Angle of attack
DSV	: Dynamic stall vortex
RHS	: Right hand side

LIST OF TABLES

LIST OF FIGURES

LIST OF SYMBOLS

k	: Reduced frequency, $\omega c/2U_\infty$
ω	: Angular frequency, rad/s
α_m	: Mean angle of attack, deg
α_0	: Amplitude of oscillation, deg
$\alpha(t)$	: Instantaneous angle of attack, deg
$\alpha_{\min}$	: Minumum angle of attack
$\alpha_{\max}$	: Maximum angle of attack
c	: airfoil chord length, m
U_∞	: Free-stream velocity, m/s
M	: Mach number, U_∞/a
a	: Speed of sound
t	: time, s
t^*	: Non-dimensional time, $U_\infty t/c$
ρ	: Density, kg/m^3
T	: Temperature, ° C
u_j	: Mass averaged velocity in the j^{th} direction
δ_{ij}	: Kronecker delta
τ_{ij}	: Shear stress tensor
μ	: Molecular viscosity,
E_t	: Total energy
q_j	: Heat flux in the j^{th} direction
k	: Thermal conductivity
γ	: Specific heat ratio
T	: Static temperature
c_V	: Specific heat at constant volume
c_P	: Specific heat at constant pressure
V	: Volume

$\hat{n}$	: Normal of the volume surface
v_g	: Volume surface velocity
S	: Surface area, reference arear
Ω	: Source terms
$\overrightarrow{F_C}$	: Convective (inviscid) flux vector
$\overrightarrow{F_D}$	: Diffusive (viscous) flux vector
q	: Velocity scale
l	: Length scale
μ_t	: Eddy viscosity
k	: Turbulent kinetic energy
ε	: Dissipation rate of kinetic energy
Re	: Reynolds number, $\rho U_\infty c/\mu$
Re_t	: Turbulent Reynolds number
y^+	: Dimensionless distance, $\rho y u_\tau /\mu$
u^+	: Dimensionless velocity, u / u_τ
T^+	: Dimensionless temperature
u_τ	: Friction velocity
τ_w	: Shear stress at wall
T_w	: Temperature at wall
q_w	: Turbulent heat flux at wall
Pr	: Prandtl number
Pr_t	: Turbulent Prandtl number
$\vec{Q}$	: Vector of conserved variables
C_n, C_N	: Normal force coefficient, $N / q_\infty S$
C_l, C_L	: Lift coefficient, $L / q_\infty S$
C_M	: Moment coefficient, $M / q_\infty Sc$
N	: Normal force
L	: Lift force
M	: Moment force
q_∞	: Dynamic pressure,(1/2) ρU_∞^2
C_{lmax}	: Maximum lift coefficient

COMPUTATIOL STUDY OF DYNAMIC STALL OVER PITCHING AIRFOILS

SUMMARY

Improved design of unmanned and/or micro air vechicles (UAV, MAV), requires increased understanding of low Reynolds number behaviour of aerodynamic surfaces. It is even more so for unsteady phenomena such as oscillating or flapping wings of small scales. Below chord Reynolds number of approximately 50,000, there is no transition to turbulence flow of laminar separation as opposed to higher Reynolds number flows where transition to turbulence results in reattachment of the flow and improve aerodynamic characteristics of the airfoil. Therefore it is important to understand low Reynolds number unsteady behaviour of airfoils in order to optimise airfoils for these flow regimes as well as high reynolds number turbulent airfoil flows. The present work consist of two main parts, laminar and turbulent flow conditions. Flowfield around a pitching airfoil is simulated by solving viscous Navier- Stokes equations in a Finite Volume discretization scheme with MUSCL approach. As the dynamic stall behaviour is of primary interest, the study in laminar flow conditions includes analyses to reveal effects of the reduced frequency, mean incidence and Reynolds number. The reduced frequency of oscillation was found to have major effect on the flow field and on the normal force coefficient of the NACA 0012 airfoil. In all turbulent flow calculations, $k-\varepsilon$ turbulence model with wall function is used to predict fully turbulent flow conditions over a pitching NACA 0015 airfoil. Three pitching airfoil cases are selected to simulate no stall, stall onset, and deep stall regimes at Re = $2\text{x}10^6$ and M = 0.3.

YUNUSLAMA YAPAN KANAT KESİTİNDE GÖRÜLEN DİNAMİK TUTUNMA KAYBININ HESAPLAMALI YÖNTEMLE İNCELENMESİ

ÖZET

İnsansız hava araçlarının daha gelişmiş tasarımı için düşük Reynolds sayılı akışların daha iyi anlaşılması gerekmektedir. Yüksek Reynolds sayılı akışlarda, akışın türbülansa geçişinden dolayı kopan akım tekrar yüzeye yapışmaktadır ve bu kanat kesitinin aerodinamik karakteristiğini artırmaktadır. Diğer taraftan laminer ayrılmadan dolayı meydana gelen bu türbülanslı akışa geçiş yaklaşık olarak Reynolds sayısının 50,000'in altında olduğu akışlarda ise görülmemektedir. Bu yüzden yüksek Reynolds sayısındaki kanat kesiti etrafındaki akışın yanısıra düşük Reynolds sayılı akışlarda da kanat kesitinin daimi olmayan davranışının anlaşılarak, bu akım koşullarına uygun optimum kanat kesitlerinin tasarımı çok önemlidir. Bu çalışmada laminer ve türbülanslı akım koşullarında yunuslama yapan kanat kesitinde görülen dinamik tutunma kaybının hesaplamalı yöntemle incelenerek, kanat kesitinin daimi olmayan davranışının anlaşılması hedeflenmiştir. Laminer akım koşullarında indirgenmiş frekans, Reynolds sayısı ve ortalama hücum açısının yunuslama yapan NACA 0012 kanat kesitinde görülen dinamik tutunma kaybına etkisi incelenmiştir. Dinamik tutunma kaybına indirgenmiş frekansın etkisinin en fazla olduğu ve Reynolds sayısının etkisinin ise en az olduğu görülmüştür. Ayrıca türbülanslı akım koşullarında yunuslama yapan NACA 0015 kanat kesitinde görülen dinamik tutunma kaybı gelişimi ise üç farklı tutunma kaybı rejimi için ayrı ayrı incelenmiştir.

1. INTRODUCTION

Stall of an airfoil in a steady case is described by a rapid drop in the lift force component, following an increase in the angle of attack that causes the flow to separate from the airfoil. The angle of attack at which this phenomenon occurs is called static stall angle. Dynamic stall, on the other hand, is a term applied in the case of a pitching airfoil, for example. In this unsteady phenomenon, the airfoil pitches through the static stall angle, while the lift continues to increase beyond its maximum steady-state value at angles well in excess of the static stall angle. This phenomenon is often associated with the formation of a leading-edge vortex, called the dynamic stall vortex, which travels along the airfoil surface as it grows, and finally separates from the airfoil at higher angles of attack.

1.1. Motivation

The problem of dynamic stall has been a topic of great interest to aerodynamicists and scientists. First, this problem presents a unique combination of unsteady effects, flow non-linearity and strong viscous-inviscid interaction, so it is an important theoretical problem. Second, it is of practical importance in various aerodynamic applications, including aircraft manoeuvrability, helicopter rotors, wind turbines, turbomachinery blades and even insect and unmanned air vehicle (UAV) wings.

The dynamic stall occurrence was first recognized on helicopter rotor blades. The significance of unsteady aerodynamics was considered by Harris and Pyrun [1], when helicopter design engineers were unable to predict the performance of high-speed helicopters using conventional aerodynamics. As a consequence of further analysis, it was observed that the additional lift on the helicopter rotor could be explained if lift on the blade was greater than that predicted by steady flow during the time when the blade was moving opposite to the direction of flight.

Simultaneously, Ham and Garelick [2] observed that this additional lift was associated with a vortex formed on the airfoil during the unsteady motion.

The performance of a helicopter is seriously restricted by the occurrence of dynamic stall on its retreating blade; it is critical to avoid the consequent accompanying strong pitching moment variations that are damaging to the vehicle. The retreating blade operates in a strongly compressible environment at a high Reynolds number and its stall is a clear case of forced, large amplitude, unsteady, flow separation. In forward flight of a helicopter, as the lifting rotor of the helicopter moves forward, the advancing blades encounter progressively higher velocities. Thus, in order to maintain its lift, the retreating blade must operate at progressively higher angles of attack as forward speed is increased. It follows that at some ratio of forward speed to rotational speed the angles of attack on the retreating blade will reach the stall [3].

1.2. Literature Survey

The challenging and difficult features of dynamic stall have stimulated its study in experimental, numerical, analytical areas.

1.2.1. Experimental investigations

While the basic features associated with the flow separation over airfoils undergoing rapid variations in angle of attack were first in the early 1930's, very little research was conducted to investigate this phenomenon until the late 1960's. Among the first to provide a theoretical description of the dynamic stall process was Ham [4]. He observed that the unsteady separation over retreating helicopter blades caused oscillatory loads on the blades that reduced the fatigue life of the rotor components. These loads were result of a sudden loss in lift due to the shedding of a large amount of vorticity at angles of attack higher than the static stall angle, a process termed dynamic stall. The conceptual description of this process offered by Ham was that dynamic stall resulted from bursting of a laminar separation bubble in the leading edge region of the airfoil. Liiva [5] conducted experiments over airfoil sections oscillating in pitch. Normal force and pitching moment calculations were made from pressure data. These results revealed that dynamic stall caused an increase in the maximum lift force and delayed stall to a higher angle of attack.

Extensive experimental tests were performed in the mid-1970's by McCroskey, McAlister and Carr [6-7]. In these studies of dynamic stall over oscillating airfoils, flow visualization and pressure measurements led the authors conclude that dynamic stall does not always result from bursting of a laminar separation bubble. The authors suggest that in some cases, it results from the forward progression of reverse-flowing fluid originating at the trailing edge, and in other cases, it results from an abrupt breakdown of the turbulent boundary layer over the forward portion of the airfoil. McAlister and Carr [8] performed detailed water tunnel flow visualizations and showed that the onset of dynamic stall begins with a rapid movement of flow reversal toward the leading edge. They state that this flow reversal originates from the trailing edge. The progression of this flow reversal creates a free shear layer between the reverse flowing fluid along the surface and inviscid free stream. This shear layer eventually becomes unstable, resulting in the development of many discrete vortices that become a single dominant stall vortex.

One of the first studies of airfoils undergoing large amplitude and constant rate pitch-up motions was performed by Walker et al. [9]. Flow visualization and near-surface hot-wire measurements were made and the results showed a strong dependence on the pitch rate. From the late 1980's through the 1990's, a great deal of research was conducted further investigating dynamic stall over both pitching and oscillating airfoils in conjunction with important advances in experimental methods and measuring capabilities of these flows. Lorber and Carta [10] were first to investigate dynamic stall over pitching airfoils at high Reynolds number. The effects of motions amplitude on dynamic stall were investigated by Chandrasekhara and Brydges [11]. Shih et al. [12] studied the unsteady flow past a pitching airfoil at constant rate by using the particle image displacement velocimetry (PIDV) technique. Shcreck et al. [13] studied the effects of pitch rate and Reynolds number on transition during the unsteady separation process.

Chandrasekhara, Carr, and others conducted a few experiments to understand the effects of compressibility on dynamic stall. In these studies, Schlieren technique and PDI were used to visualize the flow field and obtain pressure distributions over the airfoil surface. They also investigated the effects of transition and turbulence using boundary layer tripping techniques. It was found that for free-stream Mach numbers as low as 0.2; a region of local supersonic flow can exist in the leading edge of the airfoil suction surface. In some cases, shock formation in this critical region can trigger dynamic stall [14-15]. Also, Carr et al. [16] gives an extended review of experimental and computational studies about compressibility effects on dynamic stall. Moreover, it documents the major effect that compressibility can have on dynamic stall events, and the complete change of physics of the stall process that can occur as free-stream Mach number is increased.

Raffel et al. [17] and Wernert et al. [18] investigated the unsteady velocity field over NACA 0012 airfoil pitching at deep dynamic stall conditions in a low speed wind tunnel by means of PIV. In their study, the PIV velocity fields showed that the existence of a certain amount of non-reproducibility of vortex structure geometry during downstroke motion from cycle to cycle. They concluded that the extent of non-reproducibility appears to depend on the size of the separated region above the airfoil and to vary strongly with the reduced frequency.

A comprehensive experiment to investigate the dynamic stall over a pitching airfoil for a range of angles of attack including stall was conducted by Piziali [19] in the 7- by 10-Foot Subsonic Wind Tunnel at the NASA Ames Research Center. A length of 60 in. (152.4 cm) rectangular semispan wing with a 12 in. chord (30.48 cm), a NACA 0015 airfoil section, and zero twist was used to obtain both static and dynamic pressure distributions, surface flow visualizations, and supporting blockage and wall static pressure distribution. The test generated a very complete, detailed, and accurate body of data. Test data also include two-dimensional (2-D) data as well as three-dimensional (3-D) data. The dynamic data were taken for a reduced frequency range from 0.04 to 0.20 for several amplitudes of pitch oscillation about the quarter chord and over the full mean angle of attack range including both the incipient and deep stall conditions. The wing was tested with and without a leading edge upper surface boundary layer trip (BL-trip). The BL-trip consisted of a spanwise row of triangular shaped pieces of tape, 0.003 in. thickness. This trip was experimentally determined by surface oil flow studies to be the minimum disturbance required to assure consistent laminar to turbulent transition of boundary layer and elimination of the laminar leading edge bubble over the angle of attack range of the test. 100 pressure transducers are located at nine spanwise locations selected to measure the spanwise load distribution, the pressure distribution about the highly 3-D tip region, and pressure distribution of the relatively 2-D inboard region of the 3-D wing. The 2-D data are useful in developing aerodynamic computational methods for validation and also required to calibrate some of the semiemprical models. In the turbulent flow part of our study, these 2-D dynamic stall data will be used to validate our results.

1.2.2. Computational investigations

In addition to the wide range of experimental research, numerous computational studies have been conducted in the past. Dynamic stall prediction methods used by helicopter, turbomachinery, aircraft and wind turbine industries are largely based on empirical or semi-empirical approaches. Due to the extremely complicated nature of the dynamic stall phenomenon, the helicopter industry was forced to resort the development of empirical or semi-empirical methods for the prediction of dynamic stall loads. These methods are based on force and pitching moment data obtained from various wind tunnel tests. They are used as the main design parameter in the industry. These methods are being derived from on force and pitching moment data achieved from various wind tunnel tests.

Fortunately, in recent twenty years considerable progress has been made in computation of complex, unsteady, attached and separated flows using potential, boundary layer, and viscous-inviscid interaction methods and, more recently, the Euler and full unsteady Navier-Stokes equations. This development has been made possible by advances in computational methods, computing power and improved capability in modeling turbulent and transitional flows. The advantage of turbulence modeling methods is to clarify many physical flow aspects which remain unattainable by semi-empirical methods. For example, inviscid methods allow the computation of pressure lag effects in unsteady attached flows and thereby provide an explanation of observed delay in dynamic stall onset. Boundary-layer methods provide an efficient way to study the boundary-layer build up in attached flows. Viscous-inviscid interaction methods extend the efficiency of the direct boundary layer methods to cases where small regions of separated flow exist. Finally, full Reynolds-averaged Navier-Stokes equations provide a method, although a computationally expensive and time consuming one, to investigate massively separated unsteady flows.

1.2.2.1. Analytical studies

Examples of early analytical studies of different parameters describing the unsteady airfoil can be found in [20]. Ericsson and Reding [21] analyzed the dynamic stall of a helicopter blade section using a quasi-steady theory. Static experimental data was used in the theory as input to predict the dynamic stall characteristics of the airfoil. The applicability of the theory was limited by the availability of the required static experimental data. They found that the technique to be successful as long as the reduced frequency, $k = \omega c / 2U_\infty$ was not high (k < 0.5), where ω, c, U_∞ are the angular frequency of motion, airfoil chord length and free-stream velocity, respectively. Later, they improved this quasi-steady analytical method to include the transient effect of the leading-edge vortex, and thus, provided analytical means for prediction of dynamic stall characteristics at high frequency and large amplitudes [22]. Then, Ericsson and Reding [23-24] included the effects of compressibility and full scale Reynolds number in their analytical method for dynamic stall unsteady aerodynamics prediction.

1.2.2.2. Studies in laminar flow conditions

In 1977, the flow field around a NACA 0012 airfoil oscillating in pitch was analyzed by Mehta [25]. The Navier-Stokes equations in terms of the vorticity and stream function for incompressible laminar flow was solved to determine the flow field. The computations were done for two cases: Re = 5,000 and Re = 10,000. In that work, the process of dynamic stall was clearly identified. However, because these computations were very costly in computer time, only the case of high reduced frequency was analyzed. Sankar and Tassa [26] worked that dynamic stall of an NACA 0012 airfoil for laminar flow conditions by solving the compressible Navier-Stokes equations in a body-fitted coordinate system. Compressibility effects on dynamic stall were studied by computing the flow properties at Mach numbers 0.2 and 0.4 while freezing the chord Reynolds number and the reduced frequency at 5,000 and 0.5, respectively. The numerical results showed that compressibility has an inhibiting effect on the formation and growth of the leading-edge vortex. In 1989, a numerical study was conducted by Visbal and Shang [27] for laminar flow around a NACA 0015 airfoil that pitches at a constant rate to very high angle of attack. The flow field simulation was obtained by solving the full two-dimensional compressible Navier-Stokes equations on a moving grid employing an implicit approximate-factorization algorithm. The highly unsteady flow structure was found to be characterized by upstream propagation of separation from trailing edge, shedding of counterclockwise vortices into the wake, formation of a leading-edge vortex and a shear layer vortex on the leeward side, and the complex interaction of these vortices as they are being shed. The basic flow field structure for high pitch rates was shown to be in qualitative agreement with experimental data, in spite of the assumption of laminar flow. Also, they investigated that the dependence of the flow field on the pitch rate and the axis location. The flow structure around a pitching NACA 0012 airfoil around the quarter chord was numerically investigated by solving the two-dimensional compressible Navier-Stokes equations using a special matrix-splitting scheme [28]. The compressibility influence on dynamic stall was studied in detail and the influence of the Reynolds number on dynamic stall was briefly discussed. The reduced frequency was identified as a key parameter in determining the vortex wake pattern of oscillating airfoil. Reynolds number effects were found to be small compared to other parameters. The unsteady, incompressible, viscous laminar flow over a pitching NACA 0012 airfoil was simulated by Akbari et al. [29]. The dynamic stall characteristics of a pitching NACA 0012 airfoil at Reynolds numbers of 3,000 and 10^4 was studied by using a vortex method to solve two-dimensional Navier-Stokes equations in the form of vorticity and stream function, and the effects of the reduced frequency, mean angle of attack, and the location of the pitch axis were investigated. It was observed that the reduced frequency has the strongest influence on the flow field.

1.2.2.3. Studies in turbulent flow conditions

Although the investigation of dynamic stall in laminar flow still continues, the effect of turbulence on the dynamic stall was the subject of numerous numerical studies. Helicopter rotors and propeller blades as well as most turbomachinery bladings operate at Reynolds numbers above 10^5 to several millions, therefore the flow is mostly turbulent. However, there will always be a small laminar/transional region near the leading edge unless the flow is tripped close to the leading edge stagnation point. Therefore, purely laminar flow calculations are of limited practical interest.

Tuncer et al. [30] investigated the unsteady flow fields around large amplitude oscillating airfoil in incompressible turbulent flow conditions by using vorticity-velocity formulation. A viscous flow analysis and simplified vortical flow analysis, both based on an integro-differential formulation of the Navier-Stokes equations were developed and calibrated. Simulated flow fields and computed aerodynamic loads were found to be in good agreement with available experimental data. Dynamic stall of a SSC-A09 Sikorsky airfoil executing rapidly pitching and oscillatory motions was investigated numerically by Ekaterinaris [31] for turbulent $Re = 2x10^6$ flow. Turbulent flow was computed with the Baldwin-Lomax algebraic model. The lift and pitching moment hysteresis loops were predicted reasonably well from the numerical solution. In the same study the effects of compressibility and pitch rate were also investigated. It was found that dynamic stall develops at lower angles of incidence as the Mach number increases. Numerical investigations of dynamic stall in turbulent flow were also conducted by Fung and Carr [32], who concluded that an increase of the reduced frequency delays the boundary layer separation and allows the airfoil to attain higher lift values at higher angles of attack. However, at high incidences the flow becomes locally supersonic and the local supersonic region may be terminated by a shock close to the leading edge where the radius of curvature is small. They therefore suggested that the shock-generated vorticity may be responsible for dynamic stall and that compressibility effects may become important for free- stream Mach number as low as 0.2. In a later investigation, Currier and Fung [33] concluded in addition that the dependency on reduced frequency can be vastly different for airfoils with different leading-edge shape. Rizzetta and Visbal [34] examined the adequacy of Baldwin-Lomax algebraic model and $k-\varepsilon$ two equation model. An evaluation of the ability of one- and two-equation turbulence models in predicting hysteresis effects of unsteady fully turbulent flow over oscillating airfoils in the light- and deep-stall regimes was conducted by Ekaterinaris and Menter [35]. It appeared that turbulence models that tend to suppress separation perform poorly. Even though none of the models considered in the investigation was found to be capable of accurately predicting the deep-stall case, the Baldwin-Barth (B-B), the Spalart-Allmaras (S-A) and the shear stress transport (SST) $k-\omega$ models showed a significant improvement over the standard two-equation models. For light-stall case the S-A model did not yield sufficient separation and underpredicted the extreme values of unsteady loads. The B-B model overpredicted the lift drop for the light-stall case and the attached flow cases. The standard $k-\varepsilon$ and $k-\omega$ models did not predict separation even for deep-stall case. The (SST) $k-\omega$ model gave good predictions for attached and light-stall cases. It was concluded that a simple transition model significantly improves the predictions. Computations of light dynamic stall of a NACA 0012 airfoil with the Johnson-King model were conducted by Dindar and Kaynak [36]. Important differences were found between the performance of equilibrium and non-equilibrium turbulence models in light and deep dynamic stall regimes. Numerical investigations were performed by Ekaterinaris et al. [37] at the flow conditions, Re = $0.54\text{x}10^6$ and M = 0.3. It was concluded that a fully turbulent computation cannot predict the flow physics at the leading edge but a transitional flow computation closely predicted the separation bubble and the drop of the suction peak observed in experiments. In the computation the location of the transition onset was obtained by Michel's criterion, and the computation of the transitional flow region was obtained by an effective eddy viscosity. The ability of one- and two-equation turbulence models in predicting hysteresis effects of unsteady fully turbulent flow over oscillating airfoils in the light and deep stall regimes was summarized by Ekaterinaris et al. [38]. The unsteady three-dimensional flow field over an oscillating wing was investigated with the numerical solution of the compressible, time-dependent, Reynolds-averaged Navier-Stokes equations [39]. The effect of subiterations, time step and grid density on the accuracy of the computed solution was investigated.

1.3. Objectives of the Study

Improved design of unmanned and/or micro air vehicles (UAV, MAV), requires increased understanding of low Reynolds number behaviour of aerodynamic surfaces. It is even more so for unsteady phenomena such as oscillating or flapping wings of small scales. Below chord Reynolds number of approximately 50,000, there is no transition to turbulence flow of laminar separation as opposed to higher Reynolds number flows where transition to turbulence results in reattachment of the flow and improve aerodynamic characteristics of the airfoil. Therefore it is important to understand low Reynolds number unsteady behaviour of airfoils in order to optimise airfoils for these flow regimes as well as high Reynolds number turbulent airfoil flows. The present work will consist of two main parts, laminar and turbulent flow conditions.

In the laminar flow simulation part of the present study, flow field around a pitching NACA 0012 will be simulated by solving viscous Navier- Stokes equations in a Finite Volume discretization scheme with MUSCL approach (CFD-FASTRAN). As the dynamic stall behaviour is of primary interest, the study includes analyses to reveal effects of the reduced frequency, mean incidence and Reynolds number. Totally nine cases will be analyzed to investigate these key parameters on dynamic stall prediction. Calculations will be conducted for following flow conditions at Reynolds number values of 3,000 and 10,000, reduced frequency values of 0.15, 0.25 and 0.50, and mean incidence values of 15 and 20 degrees. The amplitude of oscillation is 10 degrees for all laminar cases. The laminar computational results obtained in the present study will be compared with available numerical results of Akbari [40].

In all turbulent flow calculations, $k-\varepsilon$ turbulence model with wall function will be used to predict fully turbulent flow conditions over a pitching airfoil. Three pitching airfoil cases are selected to simulate no stall, stall onset, and deep stall regimes at Re = $2x10^6$ and M = 0.3. Attached flow simulation will be performed for 4 degrees of mean angle of attack and 2 degrees of oscillation amplitude. Stall onset case will be performed at mean angle of attack of 11 degrees and amplitude of oscillation of 2 degrees. Deep stall case will be done at mean angle of attack of 13 degrees and amplitude of oscillation of 5 degrees. The turbulent computational results obtained in the present study will be compared with available experimental results of Piziali [19].

2. THEORY OF DYNAMIC STALL

2.1. The Dynamic Stall Phenomenon

Dynamic stall is investigated extensively by McCroskey and his colleagues [7] at NASA Ames Research Center in 1978. In their collection of work in this field, they helped establish a series of events that occur in most dynamic stall situations. Using various types of airfoils, the group described the process as containing 11 distinct events in Figure2.1. These events are listed here with a brief description of each. Figure 2.1 also shows the progress of C_N and C_M versus angle of attack during cycle.

(a) **Static stall exceeded**: as can be seen from the solid line (dynamic), as compared to the dashed line (static), under oscillation, the lift or normal coefficient continues to increase past the static stall value. This is one primary advantage of the unsteady motion, namely that increase in pitch rate (static stall has a pitch rate of zero) produces an overshoot in lift that increases the maximum lift coefficient, C_{Lmax} of the airfoil.

(b) **First appearance of flow reversal on surface**: close to the trailing edge, a thin layer of reverse flow appears. This thin layer does not generate the negative effects related to separation as it is contained near to the airfoil surface.

(c) **Large eddies appear in the boundary layer**: as the angle of attack is further increased, a series of eddies appear, giving the boundary layer a bumpy edge. These vortices are a foreshadowing of a much strong vortex that will eventually develop.

(d) **Flow reversal spreads over much of the airfoil chord**: in this phase, a thin sheet of reverse flow exists over the majority of the upper surface of the airfoil. Even with the existence of reverse flow, the flow remains attached and no large defect exists.

(e) **Vortex formation near leading edge**: a small protuberance appears near the leading edge. This is the origin of the dynamic stall vortex (DSV).

(f) **Lift slope increases**: due to the growth in strength and size of the DSV, there is an additional contribution to the lift, which can be thought of as a vortex lift contribution. This additional vortex lift increases the lift slope above its static stall value (the linear region of the C_L curve). Also, the presence of the vortex delays boundary layer separation from occurring.

(g) **Moment stall begins**: the existence of the vortex can be detected through a double hump in the pressure distribution on the upper (or suction) side of the airfoil. The vortex continues to grow until it sheds from the surface and is the carried downstream by the freestream velocity. As the vortex propagates over the airfoil surface, the moment is greatly decreased (a large negative pitching moment occurs). This is referred to as moment stall because it is similar to the large drop in lift during stall. This event proceeds the more traditional lift stall due to the fact that the movement of the DSV creates the moment stall, but its presence still produces the high lift. This phenomenon does not occur under static conditions and is one of the major detrimental components of the process.

(h) **Lift stall occurs**: the convection of the primary vortex results in two distinct features that contribute to lift stall. First, the loss of the vortex means that the vortex lift contribution is also lost. In addition, flow separation, which had been confined to a small thin region near the surface, is present at the leading edge and is similar to the global separation that occurs static stall. The combination of these two events creates a stall that is substantially greater in effect than the static counterpart. This event occurs when the airfoil is at the maximum.

(i) **Maximum negative moment**: as the vortex reaches the trailing edge, the moment value reaches the maximum level. A hysteresis is typically generated during the cycle. The hysteresis curve often crosses itself, created a clockwise and counter-clockwise loop. The clockwise loop represents negative damping, or energy extraction from the flow to wing. If the net damping of the cycle is negative, the amplitude of the oscillating wing will grow, unless restrained. This effect generates large torsional stresses, another major detriment to the flight performance and structure of the wing.

(j) **Full stall**: at this juncture, the flow from the leading edge is separated and a large defect region (an area of low momentum fluid) exists.

(k) **Boundary layer reattaches front to rear**: as the AoA is further decreased, the boundary layer attaches front to rear, as is the case in static stall.

(l) **Return to pre-stalled values**: this completes one cycle.

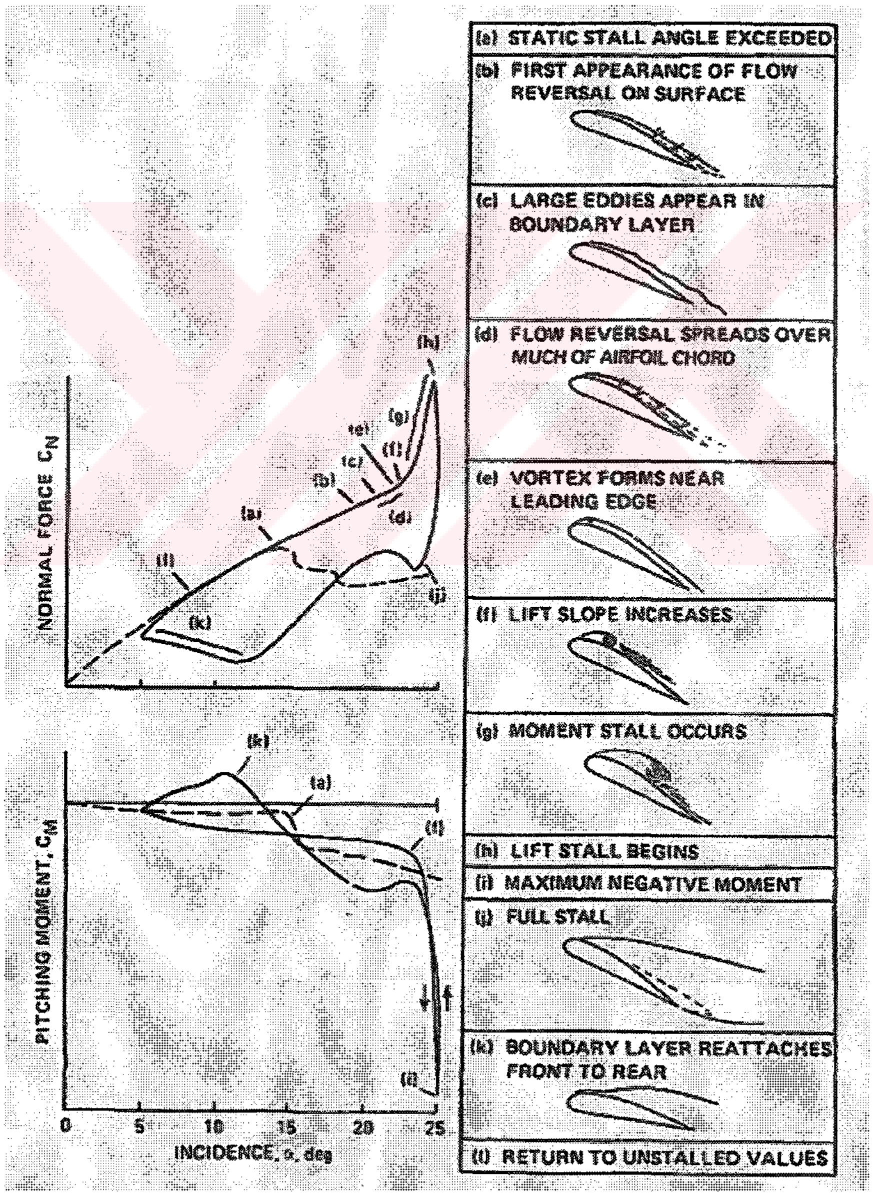

Figure 2.1: Dynamic stall events on a NACA 0012 airfoil at low free-stream Mach number [41].

To summarize, each cycle is characterized by the growth and shedding of a very strong vortex-like structure, termed the DSV. This vortex is responsible for additional lift, the delay of stall, increase of the lift slope and generating a large negative moment.

The cycle has very large hysteresis in the aerodynamic coefficients, especially C_L (or C_N). As the AoA of the airfoil begins to decrease, the section coefficients drop to much lower values that static stall case for much of the down stroke motion. This is one of the primary problems created by the dynamic stall.

The boundary layer separation of oscillating airfoils can be divided into three types: (i) separation from trailing edge towards the leading edge; (ii) abrupt breakdown of the turbulent flow on the forward portion of the airfoil and followed by initial progression of flow reversal from trailing edge to approximately the mid-chord; (iii) abrupt bursting of a leading edge laminar separation bubble. However, a dynamic stall vortex (leading edge vortex) will form at last and will dominate the features of dynamic stall no matter what type of boundary layer separation occurs [42].

2.2. Dynamic Stall Parameters

One of the reasons that dynamic stall is more difficult to analyze and predict than static stall is its dependence on a much larger number of parameters. The primary parameters are listed below in Table1.1. McCroskey [43] examined the relative importance of these parameters in influencing dynamic stall. This table is a summary of his findings.

In examining Table 1.1, we can see that three parameters play key roles in influencing dynamic stall. These three key parameters are the reduced frequency, mean angle of attack and amplitude of motion.

The reduced frequency of oscillation was found to have a major effect on the flow field and the force coefficients of the airfoil. Flow separation was delayed to higher incidences with increasing reduced frequency. The Reynolds number of the flow, on the other hand, was found to have little effect on the dynamic stall characteristics of the airfoil. Increasing the mean incidence caused flow separation to occur earlier in an oscillation cycle, even at lower angles of attack compared to a case with lower mean incidence.

Table 2.1: Effects of Dynamic Stall Parameters

PARAMETER	INFLUENCE	COMMENTS
Airfoil shape or geometry	Can be strong	Large in some cases
Mach number, M	Can be strong	Weak if M < 0.2, Strong if M > 0.2
Reynolds number, Re	Weak	Effects location of boundary layer separation
Reduced frequency, k	Strong	Key parameter
Mean angle of attack	Strong	Dynamic stall occurs when near static stall angle
Amplitude of oscillation	Strong	Should be on the order of the mean angle
Type of motion	Virtually Unknown	Cyclical motion is most common studied
3-D effects	Virtually Unknown	Very little research has been done here

Also, Carr and Chandrasekhara [16] studied the effect of compressibility on dynamic stall. Compressibility effects are observed over a wide range of Reynolds numbers and in most if not all experiments performed at free stream Mach numbers at or greater than 0.2. Compressibility can fundamentally change the physical mechanisms which cause dynamic stall to occur. Compressibility effects dramatically decrease the dynamic lift overshoot that is observed during dynamic stall at incompressible flow speeds.

2.3. Key Parameters of Dynamic Stall

As mentioned above, the reduced frequency, mean angle of attack and amplitude of motion are the key parameters of dynamic stall. They have a major effect on dynamic stall. We can define these key parameters as below. If the motion is sinusoidal, then the instantaneous angle of attack of the airfoil can be described by the following relation:

$$\alpha(t) = \alpha_m + \sin(\omega t) \qquad \textbf{(2.1)}$$

where α_m is the mean angle of attack, α_0 is the amplitude and ω is the angular frequency of motion and it is described by the following relation:

$$\omega = 2\pi f \qquad \textbf{(2.2)}$$

The reduced frequency can be written as below,

$$k = \frac{\omega c}{2U_\infty} \qquad \textbf{(2.3)}$$

where c is the airfoil chord length and U_∞ is the free-stream velocity.

When reduced frequency, k, is used in Eq. (2.1), then the equation is of the form:

$$\alpha(t) = \alpha_m + \alpha_0 \sin(2kt^*) \qquad \textbf{(2.4)}$$

where t^* is a non-dimensional time. It has the following relation

$$t^* = \frac{U_\infty t}{c} \qquad \textbf{(2.5)}$$

2.4. Dynamic Stall Regimes

By varying these three key parameters, the flow field has four distinct regimes. These four are referred to as: no stall or dynamic stall free, stall onset, light stall and deep stall, these regimes are described in Figure 2.2. If the oscillation motion lies completely below the static stall angle, then no major separation occurs. This case is referred to as 'no stall' (Figure 2.2-a).

If mean angle of attack is slightly increased, we approach the 'stall onset' scenario (Figure 2.2-b). The C_L curve essentially the same, but by examining the C_M, it can be seen that the beginning of deviations to the static case. This stall onset condition represents the limiting case of the maximum unsteady lift that can be obtained with no significant penalty in pitching moment or drag. Further increases in the maximum angle of attack produce the dynamic stall conditions described below.

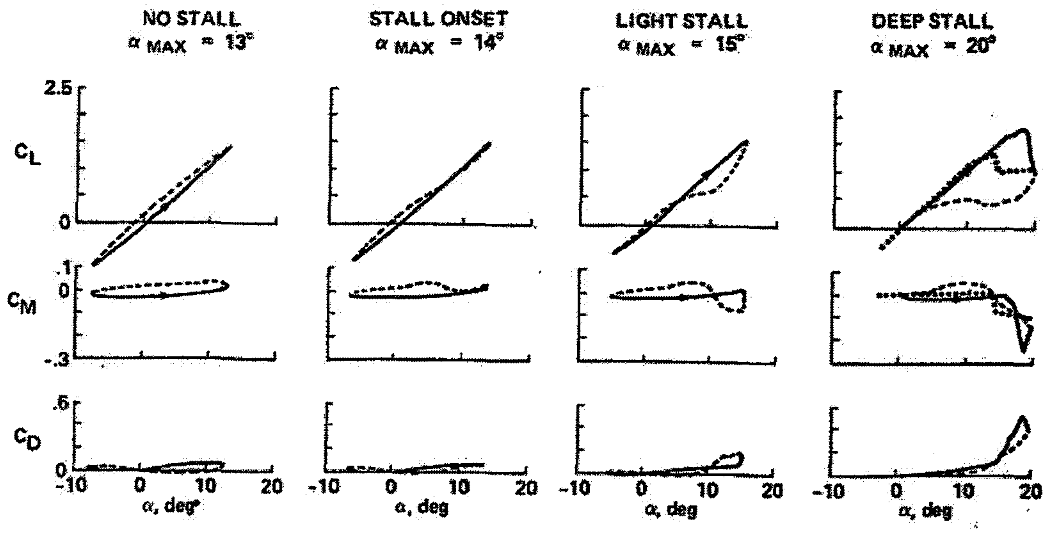

Figure 2.2: Dynamic stall regimes [44].

If mean angle of attack is slightly increased further (Figure 2.2-c), the coefficients all begin to display a distinct hysteresis. If we examine C_M curve, we can see that the cycle crosses each other. The two loops that are created represent positive damping (counter clockwise loop) and negative damping (clockwise loop). Also, the negative moment is substantially increased. This series of events is less extreme than full dynamic stall and is referred to as 'light stall'.

Figure 2.2-d shows the effects of increasing the maximum incidence to values well in excess of the static stall angle. First of all, a strong vortex-like disturbance forms in the leading edge region. Then, this vortex is shed from the boundary layer and moves downstream over the upper surface of the airfoil, producing values of C_L and C_M are very distinct according to their static counterparts when angle of attack is increasing, large amount of hysteresis occur the rest of the cycle.

The differences between light and deep stall are illustrated in Figure 2.3. As the diagram show, the qualitative features of light and deep stall vary greatly. The viscous layer region in the two cases differs by an order of magnitude. Also, while light stall experiences a trailing edge type of stall, deep stall is dominated by dynamic stall vortex presence.

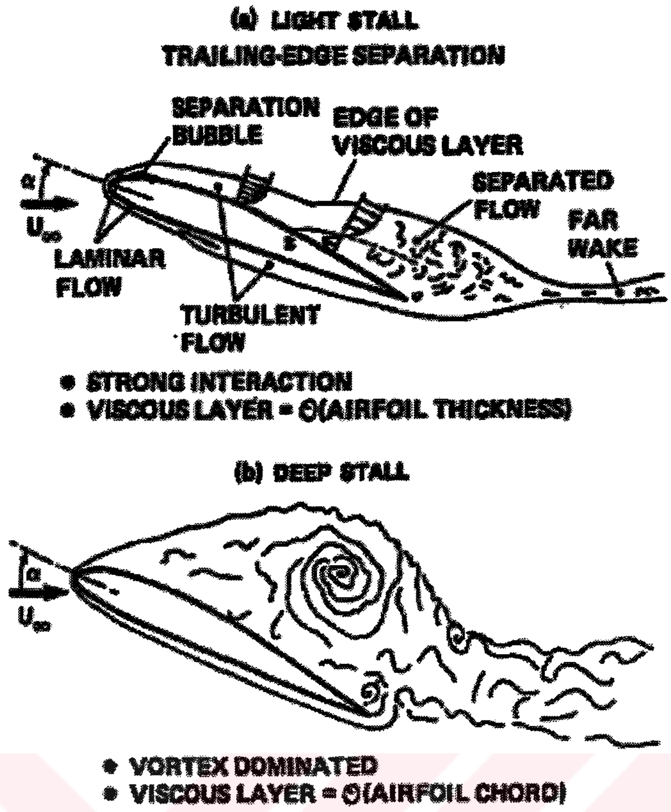

Figure 2.3: Sketch of flow field during dynamic stall [43].

3. MATHEMATICAL MODEL

3.1. Fluid Governing Equations

Typical gas dynamic equations for a fluid do not consider the motion of a control volume surrounding the fluid. To obtain proper answers for a moving body solution, the motion of the grid must be taken into account. This can be considered in a two part process. First, the standard conservation equations can be obtained for a non-moving control volume. Secondly, a transformation is applied to account for fluxes created by the movement of volumes.

3.1.1. Flow field conservation equations in a non-moving frame

The standard two dimensional conservation equations are given in this section with brief descriptions [45]. The conservation of mass is given by

$$\frac{\partial \rho}{\partial t}+\frac{\partial}{\partial x_j}(\rho u_j)=0 \tag{3.1}$$

where ρ is the density and u_j is the mass averaged velocity in the jth direction. This is the only mass conservation equation required for a calorically perfect gas.

The conservation of momentum equations are

$$\frac{\partial}{\partial t}(\rho u_i)+\frac{\partial}{\partial x_j}(\rho u_i u_j)=\frac{\partial}{\partial x_j}\left[-p\delta_{ij}+\tau_{ij}\right] \tag{3.2}$$

where p is the pressure, δ_{ij} is the kronecker delta and τ_{ij} is the shear stress tensor. For inviscid flows the terms on the right hand side of the equation are not present. The shear stress in two-dimensional can be written as

$$\tau_{ij} = \begin{bmatrix} \tau_{xx} & \tau_{xy} \\ \tau_{yx} & \tau_{yy} \end{bmatrix} \tag{3.3}$$

The shear stress tensor vector given by

$$\tau_{xx} = \frac{2}{3}\mu\left(2\frac{\partial u}{\partial x} - \frac{\partial v}{\partial y}\right) \quad , \quad \tau_{yy} = \frac{2}{3}\mu\left(2\frac{\partial v}{\partial y} - \frac{\partial u}{\partial x}\right) \tag{3.4}$$

$$\tau_{xy} = \mu\left(\frac{\partial u}{\partial y} + \frac{\partial v}{\partial x}\right) = \tau_{yx}$$

where μ is the molecular viscosity.

The conservation of total energy per volume is

$$\frac{\partial E_t}{\partial t} + \frac{\partial}{\partial x_j}[(E_t + p)u_j] = \frac{\partial q_j}{\partial x_j} + \frac{\partial}{\partial x_i}(u_j \tau_{ij}) \tag{3.5}$$

where E_t is the total energy per volume, q_j is the heat flux in the j^{th} direction. The right hand side of the equation is not present for inviscid simulations. The heat flux vector in two dimensions is given by

$$q_x = -k\frac{\partial T}{\partial x} \quad , \quad q_y = -k\frac{\partial T}{\partial y} \tag{3.6}$$

where k is the thermal conductivity of the fluid.

In addition to Eq. (3.1) through (3.6), the equation of state for perfect gases was used to close the system

$$p = (\gamma - 1)\left[E_t - \frac{1}{2}\rho(u^2 + v^2)\right] \tag{3.7}$$

where γ is the ratio of specific heats. This quantity was given a value of 1.4 assuming calorically perfect gas. The relationships for the internal energy, E_t, and the static enthalpy, h, are

$$
\begin{aligned}
E_t &= c_v T \\
h &= c_p T
\end{aligned}
\tag{3.8}
$$

where T is the static temperature, c_V is the specific heat at constant volume and c_P is the specific heat at constant pressure, respectively.

3.1.2. Flow field conservation equations for moving/deforming volumes

The previous section outlined the governing equations for flows in which the control volume was stationary or non-deforming. These equations are transformed for moving or deforming volumes by Leibnitz's Theorem.

For a general function, f, the relation ship between the time rate of change of a function integrated over a volume, the volume integration of a time derivative and the effect of moving volume surfaces is given by

$$
\frac{d}{dt}\int_V f dV = \int_V \frac{\partial f}{\partial t} dV + \int_S \overline{v_g}.\hat{n} f ds \tag{3.9}
$$

where f is the function, V is volume, t is time, v_g is the volume surface velocity. $\hat{n}$ is the normal of the volume surface and S is the surface area. Relating this theorem to the previous conservation equations, the conservation of mass is used as an example. First, the partial differentiation equation is integrated over a volume

$$
\int_V \frac{\partial \rho}{\partial t} dV + \int_V \nabla.(\rho \vec{v}) dV = 0 \tag{3.10}
$$

Applying the Divergence theorem and then Leibnitz's theorem gives

$$
\frac{d}{dt}\int_V \rho dV + \int_S \rho(\vec{v} - \overline{v_g}).\hat{n} dS = 0 \tag{3.11}
$$

In a similar fashion, all conservation equations can be manipulated such that

$$\frac{d}{dt}\int_V Q dV + \int_S (\overrightarrow{F_C} - Q\overrightarrow{v_g} - \overrightarrow{F_D}).\hat{n} dS = \int \Omega dV \tag{3.12}$$

where Q is the conserved variable vector, F_C is the convective (inviscid) flux, F_D is the diffusive (viscous) flux, v_g is the volume surface velocity and Ω are the source terms [46].

3.2. Turbulence Modeling

A variety of turbulence models are available in CFD-FASTRAN: Baldwin-Lomax, Standard k-epsilon with wall function, k-omega, Spalart-Allmaras, Menter SST. The turbulence models in CFD-FASTRAN are based on Favre averaging the equations governing the flow, given in Section 3-1. Favre averaging introduces additional term known as Reynolds stress. These stresses are modeled using Boussinessq eddy viscosity concept. The eddy viscosity is a property pf the flow, not a physical property of the fluid. Following the kinetic theory of gases, the eddy viscosity is generally modeled as the product of a velocity scale q and a length scale l,

$$\mu_t \approx \bar{\rho} q l \tag{3.13}$$

Various turbulence models differ in the way q and l are estimated. Eddy viscosity models are typically categorized by the current number of additional transport equations to be solved. The models available are zero, one, and two equation models. Zero equations use algebraic formula to relate the velocity and length scale to local mean flow conditions. These models do not explicitly consider the history of the turbulence and are the best suited for simple flows; two equation models solve transport equations for two quantities used to estimate q and l. The two equation models in CFD-FASTRAN can be further divided into high turbulent Reynolds number and low turbulent Reynolds number models. Here the qualifier "high Reynolds number" refers to the turbulent Reynolds number,

$$\mathrm{Re}_t = \frac{\rho k^2}{\mu \varepsilon} \tag{3.14}$$

where k is the turbulent kinetic energy and ε is the dissipation rate of the kinetic energy. High turbulent Reynolds models are designed for turbulent regions where the eddy viscosity is much larger than the molecular viscosity. However, viscous effects dominate the effects of turbulence in regions near solid boundaries, rendering the high Reynolds models invalid there. The common practice is to employ "wall functions" in near-wall regions and a high Reynolds turbulence model in the rest of the flow field. The wall functions are essentially an integral model connecting conditions at some distance from the wall with those at the wall.

The flow near solid boundaries consists of a viscous sublayer where the flow is directly affected by the conditions at the wall and viscous effects are much larger than turbulent effects; a buffer region where the viscous and turbulence effects are of the same order; a fully turbulent region where the effects of turbulence dominate. The thicknesses of the viscous and buffer layers and the velocity profiles within the near-wall region are important parameters in the near-wall models. Defining a dimensionless distance y^+ and velocity u^+:

$$y^+ = \frac{\rho y u_\tau}{\mu} \tag{3.15}$$

$$u^+ = \frac{u}{u_\tau} \tag{3.16}$$

The friction velocity u_τ is defined as

$$u_\tau = \left(\frac{\tau_w}{\rho}\right)^{1/2} \tag{3.17}$$

where τ_w is the shear stress at the wall.

The viscous sublayer on a smooth wall extends from the wall up to a distance of approximately $y^+ = 5$. The velocity profile in the viscous sublayer is

$$u^+ = y^+ \tag{3.18}$$

The fully turbulent region within a boundary layer typically starts at a distance from the wall of about $y^+ = 30$. Classical turbulence theories predict the velocity distribution in the fully turbulent wall region to have the form

$$u^+ = a \ln y^+ + b \tag{3.19}$$

This region is, therefore, also known as the logarithmic layer. The layer between $y^+ = 5$ and $y^+ = 30$ is commonly known as the buffer layer.

In our study, turbulence flow calculations will be done by using a two equation model, $k-\varepsilon$ turbulence model with wall function. The following section describes in detail, the $k-\varepsilon$ turbulence model used in CFD-FASTRAN [46].

3.2.1. Standard $k-\varepsilon$ model

The $k-\varepsilon$ model is a two equation model that employs partial differential equations to govern the transport of the turbulence kinetic energy, k, and its dissipation rate, ε. Several versions of the $k-\varepsilon$ model are in use today. The standard $k-\varepsilon$ model employed in CFD-FASTRAN is based on Launder and Spalding (1974).

The square root of k is taken to be the velocity scale, while the length scale is modeled as

$$l = \frac{C_\mu^{3/4} k^{3/2}}{\varepsilon} \tag{3.20}$$

The expression for eddy viscosity is

$$\mu_t = \frac{C_\mu k^2 \rho}{\varepsilon} \tag{3.21}$$

The modeled equations for k and ε are

$$\frac{\partial}{\partial t}(\rho k)+\frac{\partial}{\partial x_j}(\rho u_j k)=P-\rho\varepsilon+\frac{\partial}{\partial x_j}\left[\left(\mu+\frac{\mu_t}{\sigma_k}\right)\frac{\partial k}{\partial x_j}\right] \tag{3.22}$$

$$\frac{\partial}{\partial t}(\rho\varepsilon)+\frac{\partial}{\partial x_j}(\rho u_j \varepsilon)=C_{\varepsilon_1}\frac{P\varepsilon}{k}-C_{\varepsilon_2}\frac{\rho\varepsilon^2}{k}+\frac{\partial}{\partial x_j}\left[\left(\mu+\frac{\mu_t}{\sigma_\varepsilon}\right)\frac{\partial \varepsilon}{\partial x_j}\right] \tag{3.23}$$

with the production P defined as

$$P=\mu_t\left(\frac{\partial u_i}{\partial x_j}+\frac{\partial u_j}{\partial x_i}-\frac{2}{3}\frac{\partial u_m}{\partial x_m}\delta_{ij}\right)\frac{\partial u_i}{\partial x_j}-\frac{2}{3}k\frac{\partial u_m}{\partial x_m} \tag{3.24}$$

where σ_k and σ_ε are effective “Prandtl numbers” which relate eddy diffusion of k and ε to the momentum eddy viscosity.

The five empirical constants in these model relations have the following recommended values for attached boundary-layer calculations:

$$C_\mu=0.09 \quad C_{\varepsilon_1}=1.44 \quad C_{\varepsilon_2}=1.92 \quad \sigma_k=1.0 \quad \sigma_\varepsilon=1.3 \tag{3.25}$$

The standard $k-\varepsilon$ model is a high Reynolds model and in not intended to be used in the near wall regions where viscous effects dominate the effect of turbulence. Wall functions are used in cells adjacent to walls. The k and ε transport equations are not numerically integrated in these cells. Instead, semi empirical expressions are used to relate k, ε and the friction velocity u_τ. These expressions are obtained from analysis of the momentum and turbulence equations for a flat plate boundary layer, assuming a logarithmic velocity profile.

$$k=\frac{u_\tau^2}{\sqrt{C_\mu}} \tag{3.26}$$

$$\varepsilon = \frac{C_\mu^{\frac{3}{4}} k^{\frac{3}{2}}}{\kappa y} \tag{3.27}$$

In the standard wall function approach employed by CFD-FASTRAN, the wall shear stress is obtained by assuming the velocity profile between the wall and the first grid point away from the wall obeys the following law of the wall:

$$u^+ = y^+ \ \ for\ y^+ < 11.5 \tag{3.28}$$

$$u^+ = \frac{1}{\kappa}\ln(Ey^+)\ \ for\ y^+ > 11.5 \tag{3.29}$$

The wall shear stress is calculated iteratively from the known values of y and u in the fist cell. The constants appearing in the equations above are experimentally determined to be $E = 9.0$ and $\kappa = 0.41$. Because the semi-empirical relations for k and ε in the first cell assume a logarithmic velocity profile, the turbulence wall functions are strictly valid only if the center of the cell nearest the wall is inside the logarithmic boundary layer ($y^+ > 30$).

The wall shear stress evaluated using equation Eq. (3.24) and Eq. (3.24) is used to calculate the boundary condition for the velocity components parallel to the wall. Similarly, the turbulent heat flux at the wall is obtained by assuming a profile for temperature in the near-wall region.

The velocity and temperature profiles are assumed to be similar when plotted in wall coordinated (Reynolds analogy). The dimensionless temperature is defined as

$$T^+ = \left(\frac{T_w - T \rho C_p u_\tau}{q_w} \right) \tag{3.30}$$

where T and T_w are the temperature in the first cell and the wall, respectively; C_p is the fluid heat capacity; and q_w is the turbulent heat flux at the wall.

T^+ at the first grid point is obtained from a thermal law of the wall,

$$T^{+} = \Pr y^{+} \quad for \quad y^{+} \leq y_{I}^{+} \tag{3.31}$$

$$T^{+} = \frac{\Pr_t}{k} \ln y^{+} + A(\Pr) \quad for \quad y^{+} \geq y_{I}^{+} \tag{3.32}$$

where $\Pr_t$ is the turbulent Prandtl number and $A(\Pr) = 13\Pr^{2/3} - 7$ which is valid for $\Pr \geq 0.7$. The intersection of Eq. (3.26) and Eq. (3.27) occurs at y_I^{+} [46].

3.3. Flow Field Numerical Method

The partial differential equations given by the governing equations have no known general analytical solution. This requires that numerical techniques be employed to solve for the unknowns. In this chapter, the approach by used CFD-FASTRAN to discretize the equations both spatially and temporally to obtain a solution for a given geometric configuration will be described [46].

3.3.1. Finite volume and temporal discretization

The governing equations presented in Section 3.1 can be expressed in vector notation with some appropriate closure models such that

$$\frac{\partial Q}{\partial t} + \nabla . \overrightarrow{F_C} - (\nabla . \overrightarrow{F_D}) = 0 \tag{3.33}$$

where Q is the vector of conserved variables, defined as

$$\vec{Q} = \begin{bmatrix} \rho \\ \rho u \\ \rho v \\ E_t \end{bmatrix} \quad \overrightarrow{F_C} = F_C \hat{i} + G_C \hat{j} \qquad \overrightarrow{F_D} = F_D \hat{i} + G_D \hat{j} \tag{3.34}$$

where C represents convection and D represents diffusion.

The convective flux $\overrightarrow{F_C}$ is taken as

$$\overrightarrow{F_C} = \begin{bmatrix} \rho u \\ \rho u^2 + p \\ \rho uv \\ (E_t + p)u \end{bmatrix} \qquad \overrightarrow{G_C} = \begin{bmatrix} \rho v \\ \rho vu \\ \rho v^2 + p \\ (E_t + p)v \end{bmatrix} \tag{3.35}$$

The diffusive flux, $\overrightarrow{F_D}$, is

$$\overrightarrow{F_D} = \begin{bmatrix} 0 \\ \tau_{xx} \\ \tau_{xy} \\ u\tau_{xx} + v\tau_{yy} - q_x \end{bmatrix} \qquad \overrightarrow{G_D} = \begin{bmatrix} 0 \\ \tau_{yx} \\ \tau_{yy} \\ u\tau_{yx} + v\tau_{yy} - q_y \end{bmatrix} \tag{3.36}$$

To discretize the flow field governing equations for a moving volume

$$\frac{d}{dt}\int Q dV + \int \nabla \bullet \overrightarrow{F_C} - Q\overrightarrow{v_g} - \overrightarrow{F_D} dV = SdV \tag{3.37}$$

Applying the Divergence theorem gives

$$\frac{d}{dt}\int Q dV + \int (\overrightarrow{F_C} - Q\overrightarrow{v_g} - \overrightarrow{F_D}) dA = SdV \tag{3.38}$$

For a grid that is comprised of discrete volumes and areas, the equation above is transformed to:

$$\frac{\partial (QV)}{\partial t} + \sum_{f=1}^{N\,face} (\overrightarrow{F_C} - Q\overrightarrow{v_g} - \overrightarrow{F_D})_f^{n+1} \bullet \hat{n}_f^{\,n+1} \Delta A_f^{n+1} \tag{3.39}$$

Note "n+1" represents the next time level which means that the above discretized equation is valid for implicit schemes. Also allow

$$\overrightarrow{F_{cm}} = \overrightarrow{F_C} - Q\overrightarrow{v_g} \tag{3.40}$$

where

$$
\begin{aligned}
cm &= convective-moving \\
\hat{n} &= the\,cell\,face\,normal \\
\Delta A_f &= the\,cell\,face\,area \\
\Delta V &= the\,cell\,volume
\end{aligned}
$$

The flux and source vector must be linearized to estimate the fluxes and sources at n+1.

This gives (temporarily dropping some subscript for shortness)

$$F_f^{n+1} = F_f^n + \left.\frac{\partial F_f}{\partial Q}\right|_f \Delta Q \tag{3.41}$$

and

$$S_{cell}^{n+1} = S_{cell}^n + \left.\frac{\partial S}{\partial Q}\right|_{cell} \Delta Q \tag{3.42}$$

$$\delta QV = V^{n+1}\Delta Q^n - Q^n \delta V^n \tag{3.43}$$

$\frac{\partial F_f}{\partial Q}$ and $\frac{\partial S}{\partial Q}$ are the flux jacobian and source jacobian, restively.

Rearranging terms gives

$$
\begin{aligned}
&\frac{\Delta Q}{\Delta t}\Delta V^{n+1} + \sum_{f=1}^{N\,face}\left[\left(\left.\frac{\partial \overrightarrow{F_{cm}}}{\partial Q}\right|_f^n - \left.\frac{\partial \overrightarrow{F_D}}{\partial Q}\right|_f^n\right)\Delta Q \bullet \hat{n}_f \Delta A_f\right] \\
&-\left(\Delta V \frac{\partial S^n}{\partial Q}\right)\Delta Q = S\Delta V^{n+1} - \sum_{f=1}^{N\,face} F_f^n \bullet \hat{n}_f \Delta A_f + Q^n \delta V^n
\end{aligned}
\tag{3.44}
$$

For explicit schemes, the second and third terms of the left hand side are not required. For non-moving grids $\delta V^n = 0$, $\Delta V^{n+1} = V^n$, and $\Delta A^{n+1} = \Delta A^n$.

3.3.2. Spatial discretization

The flux vector and flux jacobians must be evaluated. CFD-FASTRAN is based on idea of upwind schemes for the convective (convective-moving) fluxes. In particular, two different flux schemes are available. The first scheme is based on Roe's approximate Riemann solver and is considered a flux difference scheme. The second approach is based on Van Leer's scheme and is considered to be a flux vector splitting algorithm. Both Roe's and Van Leer's schemes are first order spatially accurate. However this limitation may be overcome with the use of limiter.

Roe's flux difference scheme will be used with Osher-Chakravarthy limiter in our computations, therefore a brief description of this scheme and limiter will be given below. For the other limiters (Minmod and monotonic Van-Leer) and Van Leer's scheme, a brief description can be found in [45].

The "convective-moving" flux for Roe's scheme is given by

$$F^{*n}_{cm,f} = \frac{1}{2}\left[F^{n}_{cm}(Q^{L}) + F^{n}_{cm}(Q^{R})\right] - \frac{1}{2}\left|\tilde{A}_F\right|(Q^{R} - Q^{L}) = F^{*}_{f}(Q^{L}, Q^{R}) \qquad \textbf{(3.45)}$$

where

$*$	$=$ *the numerical flux*
L	$=$ *left states*
R	$=$ *right states*
$\tilde{A}_F$	$=$ *the Roe – average flux jacobian*

The linearized numerical flux is

$$F^{*n+1}_{cm,f} \cong F^{*n}_{cm,f} + \left.\frac{\partial F^{*}}{\partial Q^{L}}\right|^{n}_{f} \Delta Q^{L} + \left.\frac{\partial F^{*}}{\partial Q^{R}}\right|^{n}_{f} \Delta Q^{R} \qquad \textbf{(3.46)}$$

The second and third right hand terms replace $\left.\frac{\partial F}{\partial Q}\right|^{n}_{f} \Delta Q$ in the discretized governing equations. The Roe averaged variables are taken to be

$$\tilde{\rho} = \sqrt{\rho_i \rho_{i+1}} \ \ or\ \ \tilde{\rho} = \sqrt{\rho_{cell} \rho_{neighbor}} \tag{3.47}$$

Let's take the following relation for structured and unstructured grids, respectively

$$R = \sqrt{\frac{\rho_{i+1}}{\rho_i}} \ \ or\ \ R = \sqrt{\frac{\rho_{neighbor}}{\rho_{cell}}} \tag{3.48}$$

Other variables may be Roe-average such as

$$\tilde{u} = \frac{Ru_{i+1} + u_i}{R+1}, \text{ etc.} \tag{3.49}$$

The flux jacobian $\tilde{A}_F$ can be evaluated by

$$\tilde{A}_F = \frac{\partial F}{\partial Q} = \frac{\partial Q}{\partial q}\left(\frac{\partial q}{\partial Q}\frac{\partial F}{\partial q}\right)\frac{\partial q}{\partial Q} = MA^{"}M^{-1} \tag{3.50}$$

where q is the vector of primitive variables

$$\left[E_{\text{int}},\ \rho,\ u,\ v,\ p\right]^T \tag{3.51}$$

The Osher-Chakravarthy limiter is

$$\psi(r) = \frac{1}{2}[(1-\kappa)\min\text{mod}(\beta, r) + (1+\kappa)\min\text{mod}(1, \beta r) \tag{3.52}$$

where

$$\beta = \min\left(\frac{3-\kappa}{1-\kappa}, \frac{3+\kappa}{1+\kappa}\right) \tag{3.53}$$

The value of κ determines the accuracy. For $\kappa = \frac{1}{3}$, the Osher-Chakravarthy limiter is third order spatially accurate. The diffusive flux, F_D, must also be determined for viscous problems.

From the formula of viscous flux, one can observe that the viscous flux is not only a function of the conservative variables but also the function of velocity and temperature gradients. Since, the viscous flux is discretized using central differencing, the flow variable Q vector and transport properties (k, μ) at a cell surface can be calculated using simple weighted averages between the cell center values to the left and right of the face. More detailed calculation procedure can be found in [45].

3.3.3. Flow field solution procedure

The solution for the discretized equation is achieved by a time marching algorithm. For steady flows, the time marching scheme is repeated until residuals or the change is the solution of the solution variables fall below a tolerance level. The time marching scheme produces a time-accurate answer for a transient and unsteady simulation. One explicit and two implicit time marching schemes are available in CFD-FASTRAN: multi-stage Runge-Kutta scheme, block diagonal implicit scheme, jacobi iterative implicit scheme.

The block diagonal implicit scheme approach used in our computations is essentially a subset of the Jacobi point iterative procedure (see theory manual for brief description of jacobi point iterative procedure). The discretized equation is

$$\left[\frac{\Delta V}{\Delta t} + \sum_f \left(\frac{\partial \vec{F}_{cm}}{\partial Q_i}\Bigg|^n - \frac{\partial \vec{F}_D}{\partial Q_i}\Bigg|^n \right) \bullet \hat{n} \Delta A_f - \Delta V^{n+1} \frac{\partial S}{\partial Q_i}\Bigg|^n \right] \Delta Q = RHS(Q) \tag{3.54}$$

where

$$RHS(Q) = S_i \Delta V^{n+1} - \sum_f F_f^n \bullet \tilde{n}_f \Delta A_f + Q_i^n \delta V_i^n \tag{3.55}$$

It must be noted that all of diagonal terms have been neglected which leaves the main block-diagonal. This scheme is not time accurate.

3.4. Flow Solver and Motion Model

The solutions of the present study are performed by using the CFD-FASTRAN solver in time accurate mode [46]. Some flow solver options used in this study are as follows:

- High-order Roe flux difference splitting with Osher-Chakravarthy limiter
- Backward Euler time integration
- Fully implicit scheme with implicit convergence of 10^{-4}

CFD-FASTRAN also employs a prescribed motion model capability for simulating bodies with known or prescribed motion. The model is coupled with the Navier-Stokes flow solver to provide aerodynamic analysis for bodies in relative motion. The salient features of this module include:

- Fully integrated into flow solver
- Arbitrary motion for displacement, velocity or acceleration using 5th order polynomials, sine-cosine polynomials or input from a time profile file
- Motion may be prescribed in inertial or any body-fixed coordinate system
- Motion models may have dependencies and sequencing

In our calculations, the angular displacement of the computational domain is defined by the sine/cosine polynomial option in the solver.

CFD-FASTRAN solver is supported by an extensive framework of tools for pre and post processing. CFD-GEOM is a general-purpose geometry and grid generation system. Structured C-grids in the turbulent flow simulations are generated by using CFD-GEOM. CFD-VIEW is an interactive graphics program for post-processing numerical results from CFD-FASTRAN. In the present study, animations of pitching airfoils cases and plots of streamline patterns at instantaneous angle of attacks are gotten by CFD-View.

3.5. Implementation of Boundary Conditions

Boundary conditions implemented on C-grid computational domain in our simulations are shown in the Fig.3.1.

Viscous wall boundary condition is implemented on the airfoil surface (see Fig. 3.1). For a viscous surface, the normal and tangential velocities are set to be equal to the grid velocity (or boundary velocity) at that point. This means for non-moving walls $\vec{v}=0$, while for moving walls $\vec{v}=\vec{v}_g$. These conditions enforce impermeable conditions for mass and momentum. For a calorically perfect gas, there are four subtypes in CFD-FASTRAN: adiabatic, isothermal, specified heat flux, and radiative. In our calculations, adiabatic subtype is used. The adiabatic condition enforces $q_w=0$. This relationship can be reduced to $T_w=T_c$ which states that local wall temperature is equal to the cell temperature adjacent to the wall.

The adiabatic conditions are:

$$\begin{aligned} p_w &= p_c \\ u_w &= u_g \\ v_w &= v_g \\ T_w &= T_c \end{aligned} \tag{3.47}$$

Wall density, ρ_w is computed using p_w, T_w and the thermal equation of state.

Outlet boundary condition is implemented at the exit domain (see Fig.3.1). Outlet boundary condition has two options in CFD-FASTRAN: fixed static pressure (Fixed P) and extrapolated. In our calculations, fixed static pressure option is selected. For subsonic outflows, the Fixed P option can be used and requires the pressure on the outlet plane of a domain. CFD-FASTRAN checks the local Mach number at boundary points using Fixed P conditions. For local subsonic outflow, the pressure is set by input value in the solver while remaining flow variables are extrapolated from the interior to the outlet plane.

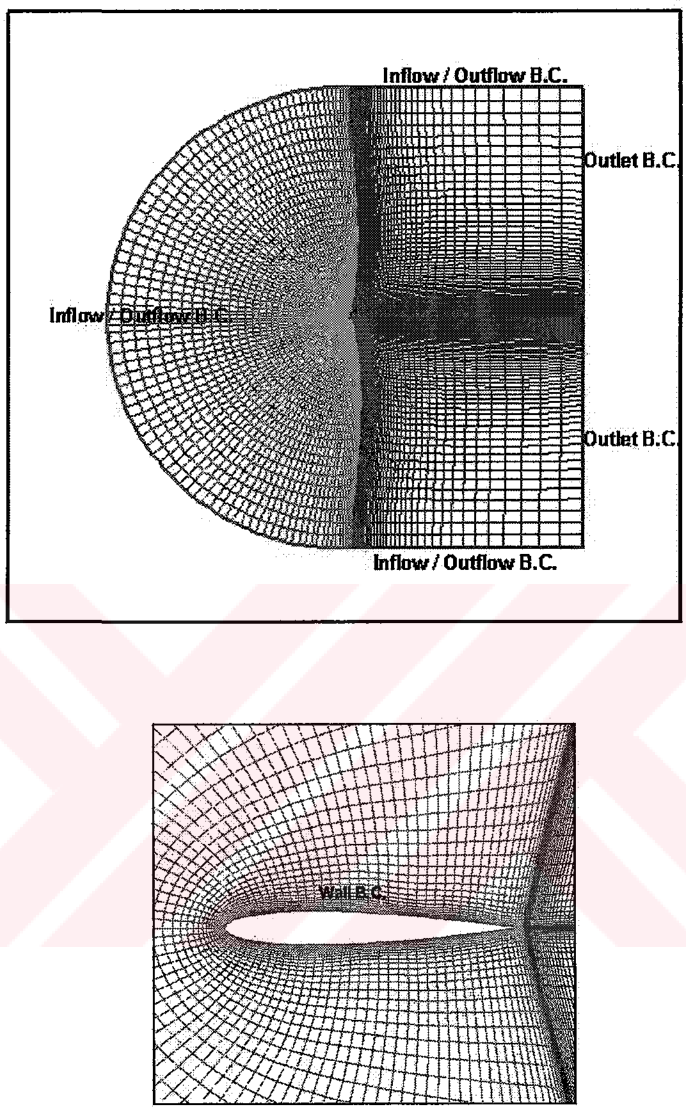

Fig.3.1: Boundary conditions on the airfoil and outer sides of the domain.

As it can be seen in Fig. 3.1, inflow/outflow boundary condition is implemented at inlet domain. Inflow/Outflow boundary condition in CFD-FASTRAN is a combination of inlet and outlet boundary conditions. For subsonic outflow, this boundary condition behaves as the Fixed P Outlet boundary condition. The static pressure set by input is maintained on the boundary while other variables are extrapolated from the interior [45].

4. RESULTS AND DISCUSSION

Considered case-studies in this study consist of pitching NACA 0012 airfoil cases in laminar flow conditions and pitching NACA 0015 airfoil cases in turbulent flow conditions. In all case-studies, before proceeding with unsteady flow computations, a steady-state solution is obtained at the mean incidence, using free stream conditions as initial solution. Then, the converged solution is used as an initial condition for the unsteady computations. For all simulation cases, the unsteady periodic solution is obtained after three cycles.

4.1. Computational Domain

A structured C-grid, as it can be seen in Figure 4.1, consisting of 240x70 cells is employed for laminar calculations at Re=10,000. It is generated by using Blazek's elliptic mesh generator [47]. Farfield boundary is extended 10 chord lengths from airfoil surface. The airfoil chord length is about $c = 4.1 \times 10^{-3}$ m and the initial wall spacing is 5×10^{-4}c.

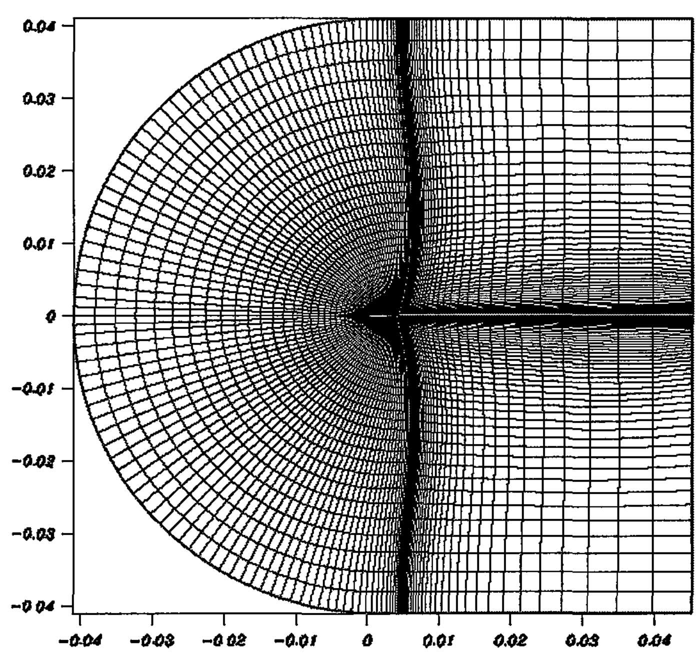

Fig.4.1: View of computational domain (Re=10,000).

At Re=3,000, the airfoil chord length is about 1.23×10^{-3} m at the same flow conditions as Re = 10,000. A structured C-grid with 240x70 cells is generated again by using Blazek's elliptic mesh generator. Farfield boundary is about 20 chord lengths away from airfoil. The initial wall spacing is about 5×10^{-4}c.

4.2. Dynamic Stall in Laminar Flow Conditions

In this section, results obtained from our laminar flow simulation cases over a pitching NACA 0012 airfoil are presented, and the effects of some parameters on dynamic stall characteristics of the airfoil are investigated.

Sinusoidal oscillations of the airfoil between $\alpha_{\min} = 5^\circ$ and $\alpha_{\max} = 25^\circ$, or between $\alpha_{\min} = 10^\circ$ and $\alpha_{\max} = 30^\circ$, at reduced frequencies of k = 0.15, 0.25, and 0.5, are considered. Reynolds number of flow is set at Re = 10,000 or Re = 3,000. It should be noted that in this range of Reynolds number, the boundary layer and the near wake are not considered to be turbulent.

A summary of these case-studies for a pitching NACA 0012 airfoil in laminar flow conditions is presented in Table 4.1. As it can be seen in this table, more emphasis is put on the effects of the reduced frequency, k , in our study. Besides the reduced frequency, the effects of Reynolds number and mean angle of attack are also studied, in three groups (A to C). Our results will be compared with computational data performed by Akbari [40].

Group A: reduced frequency effects

In cases 1 to 3, the airfoil pitches about the quarter-chord between $\alpha_{\min} = 5^\circ$ and $\alpha_{\max} = 25^\circ$, and Reynolds number is set at $Re = 10^4$. The reduced frequency in cases 1 to 3 is 0.15, 0.25 and 0.50, respectively. Three oscillation cycles of the airfoil are simulated in each case.

Case 1: In this case, with k = 0.15, the normal force coefficient (C_n) continues to increase in the upstroke part of the cycle, until $\alpha \approx 22^\circ$ when $C_n \approx 1.97$. The normal force (C_n) coefficient for this case is shown in Figure 4.2.

Table 4.1: List of laminar flow simulation cases.

GROUP	CASE	Reynolds Number, Re	Mean angle of attack, α_m(deg)	Amplitude of oscillation, α_0(deg)	Reduced frequency, k	Pitch axis location
A	1	10,000	15	10	0.15	c/4
	2	10,000	15	10	0.25	c/4
	3	10,000	15	10	0.50	c/4
B	4	3,000	15	10	0.15	c/4
	5	3,000	15	10	0.25	c/4
	6	3,000	15	10	0.50	c/4
C	7	10,000	20	10	0.15	c/4
	8	10,000	20	10	0.25	c/4
	9	10,000	20	10	0.50	c/4

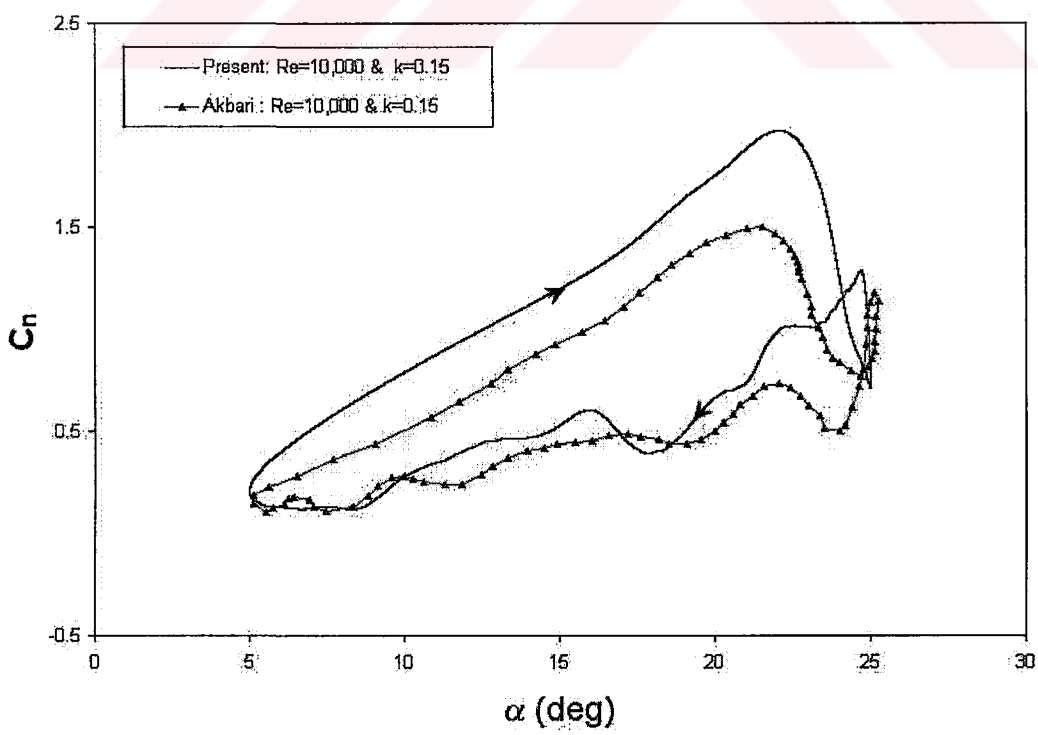

Figure 4.2: The hysteresis loop for normal force coefficient (Re = 10,000, k = 0.15).

Case 2: In this case, where the reduced frequency is set at k = 0.25, the normal force coefficient (C_n) continues to increase with the incidence up to α_{max} during the upstroke, unlike in case 1 in which the peak in C_n occurs before α_{max} is reached. The maximum value of C_n is at about 2.1 in this case, which is higher compared to case 1. The normal force (C_n) coefficient for this case is plotted in Figure 4.3.

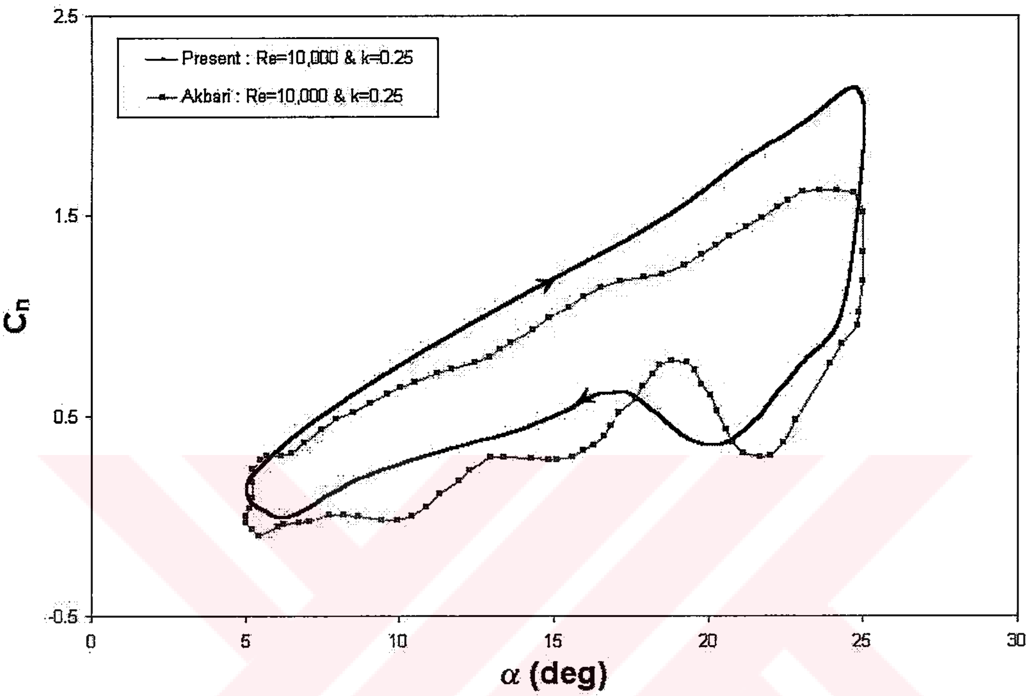

Figure 4.3: The hysteresis loop for normal force coefficient (Re = 10,000, k = 0.25).

Comparing the results of cases 1 and 2, it is observed that the sudden drop seen in Case 1 during the upstroke near the maximum incidence in the normal force coefficient is eliminated with the increasing the reduced frequency.

Case 3: The normal force coefficient for this case, with k = 0.50, is plotted in Figure 4.4. In this higher frequency case the normal force coefficient curve is smoother compared to the other cases. The maximum value of C_n is about 1.89 and occurs at around α_{max}. In the downstroke part of the cycle of Case 3, the normal force is always less than that in the upstroke part for the same incidences. In fact, the normal force takes even negative values during the downstroke with a minimum value of about -0.135 at $\alpha \approx 6.34°$.

Comparing the results of the three cases in group A, it can be concluded that increasing the reduced frequency can slightly increase the normal force 'overshoot' up to a limit, after which any more increase in the reduced frequency has no apparent effect on this overshoot. However, an increase in the reduced frequency has some effects on the general profile of the normal force coefficient loop. The minimum value of the normal force coefficient decreases with increasing reduced frequency. The comparisons of normal force coefficients of three cases are plotted in Figure 4.5.

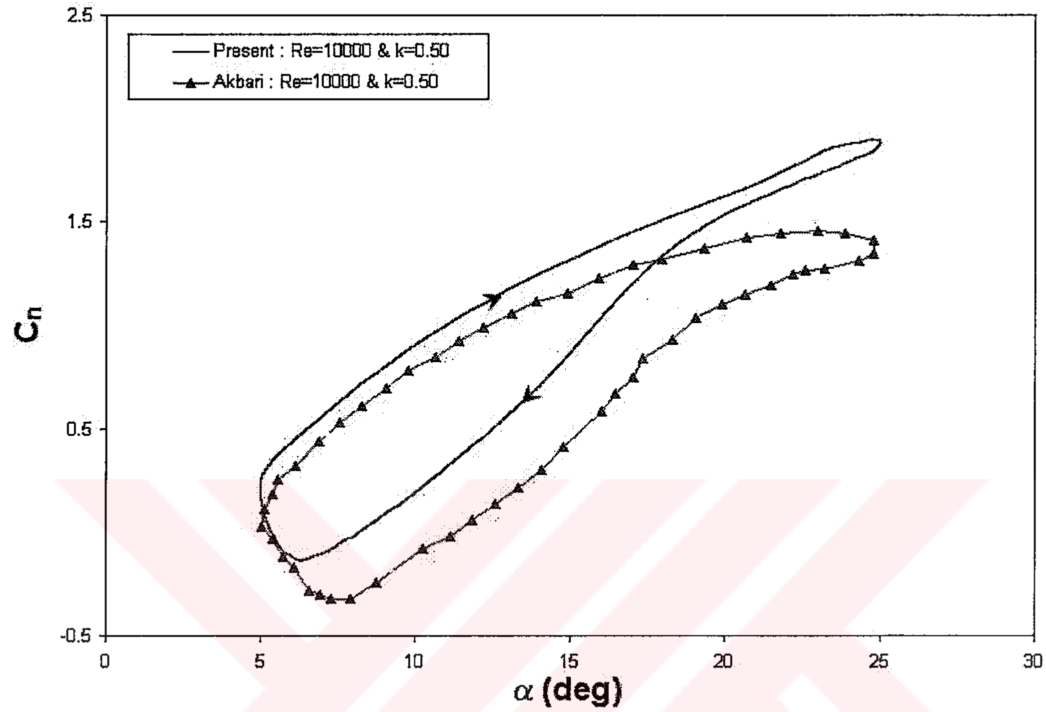

Figure 4.4: The hysteresis loop for normal force coefficient (Re = 10,000, k = 0.50).

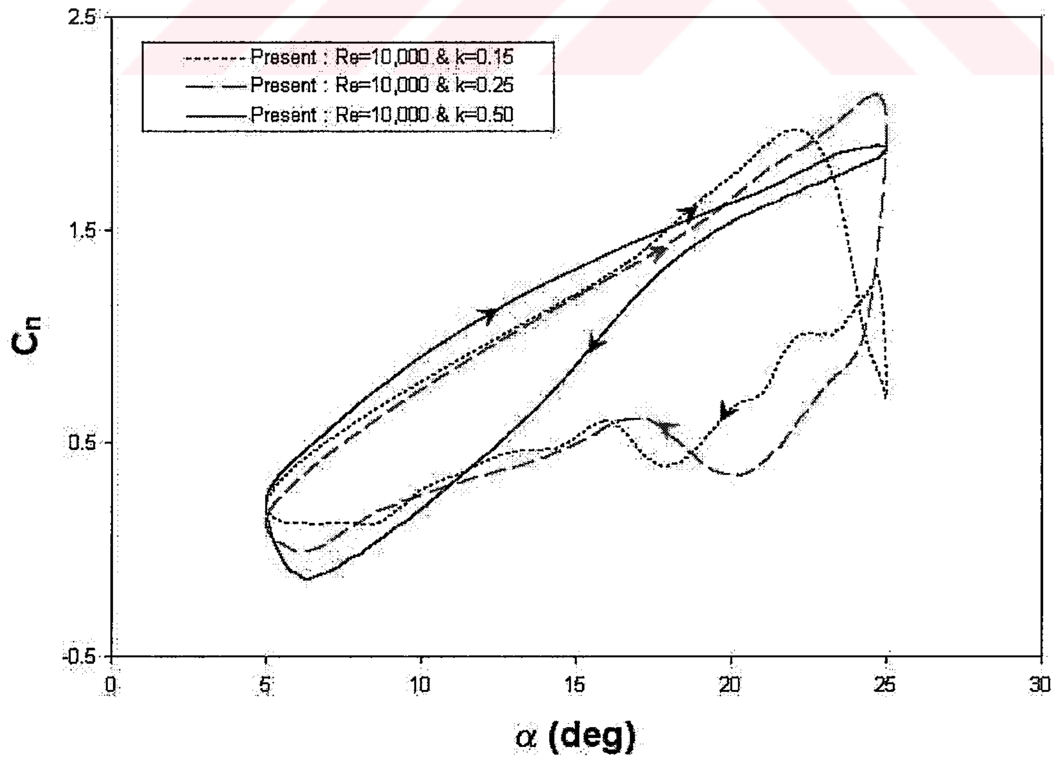

Figure 4.5: Comparison hysteresis loops for normal force coefficient (Re =10,000).

Streamline patterns at several incidences during the upstroke and downstroke at reduced frequency of k = 0.15 are shown below in Figure 4.6.

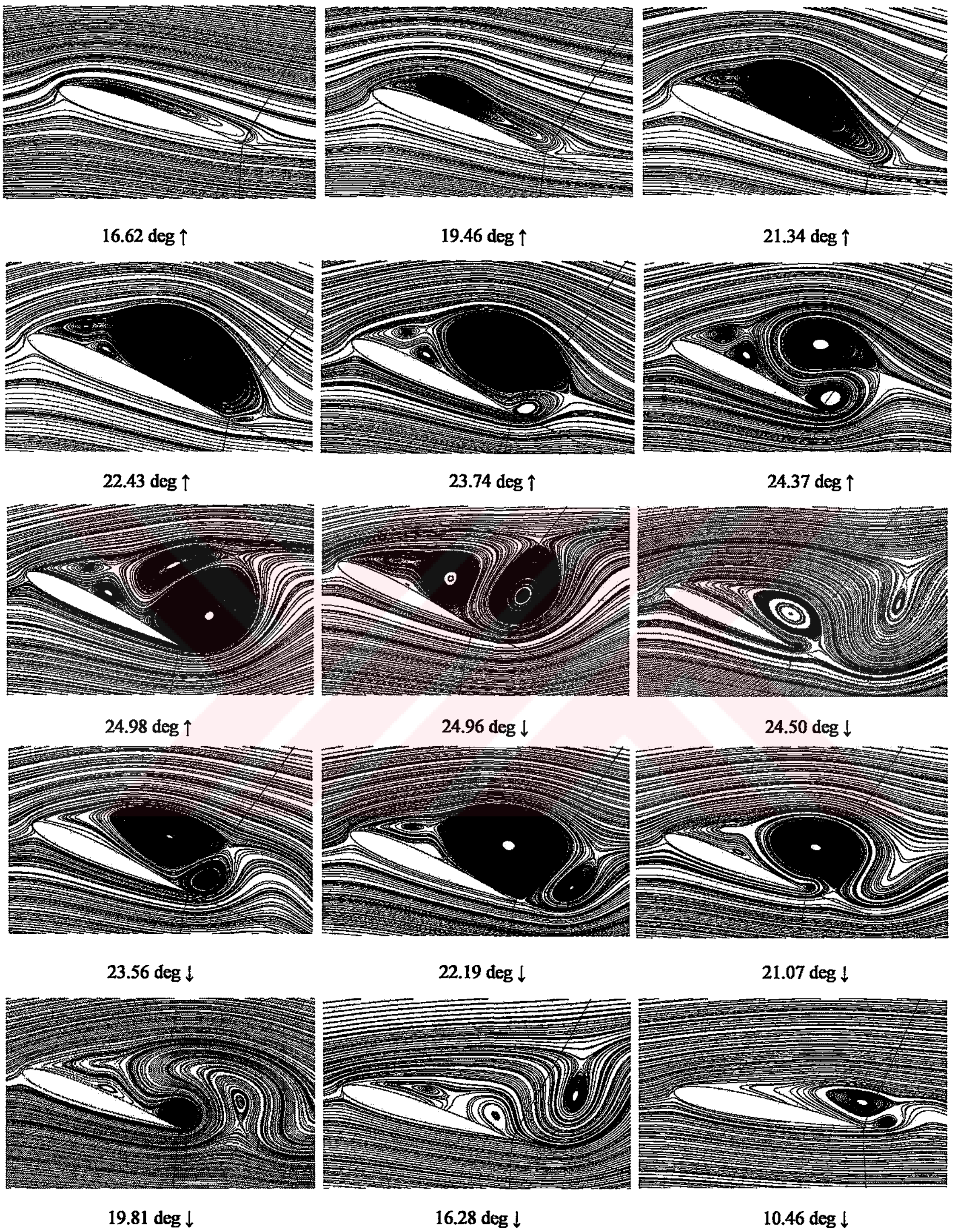

Figure 4.6: Streamline patterns at several angles of attack during upstroke (↑) and downstroke (↓) motions for a pitching NACA 0012 airfoil, at k = 0.15, $\alpha_0 = 10^\circ$, $\alpha_m = 15^\circ$, pitching axis at c/4, and $\mathrm{Re} = 10^4$.

Streamline patterns at several incidences during the upstroke and downstroke at reduced frequency of k = 0.25 are shown below in Figure 4.7.

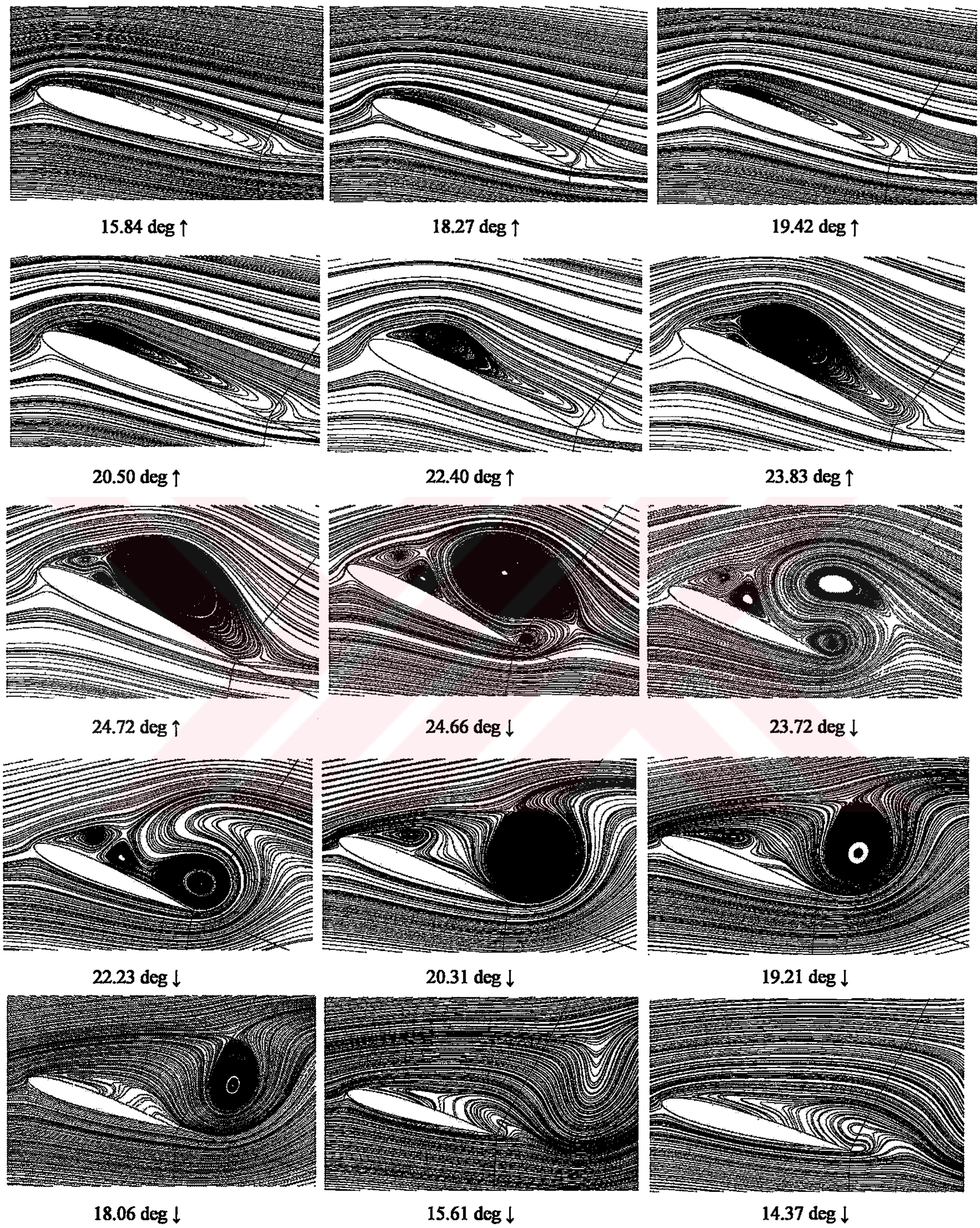

Figure 4.7: Streamline patterns at several angles of attack during upstroke (↑) and downstroke (↓) motions for a pitching NACA 0012 airfoil, at k = 0.25, $\alpha_0 = 10^\circ$, $\alpha_m = 15^\circ$, pitching axis at c/4, and $\mathrm{Re} = 10^4$.

Streamline patterns at several incidences during the upstroke and downstroke at reduced frequency of k = 0.50 are shown below in Figure 4.8.

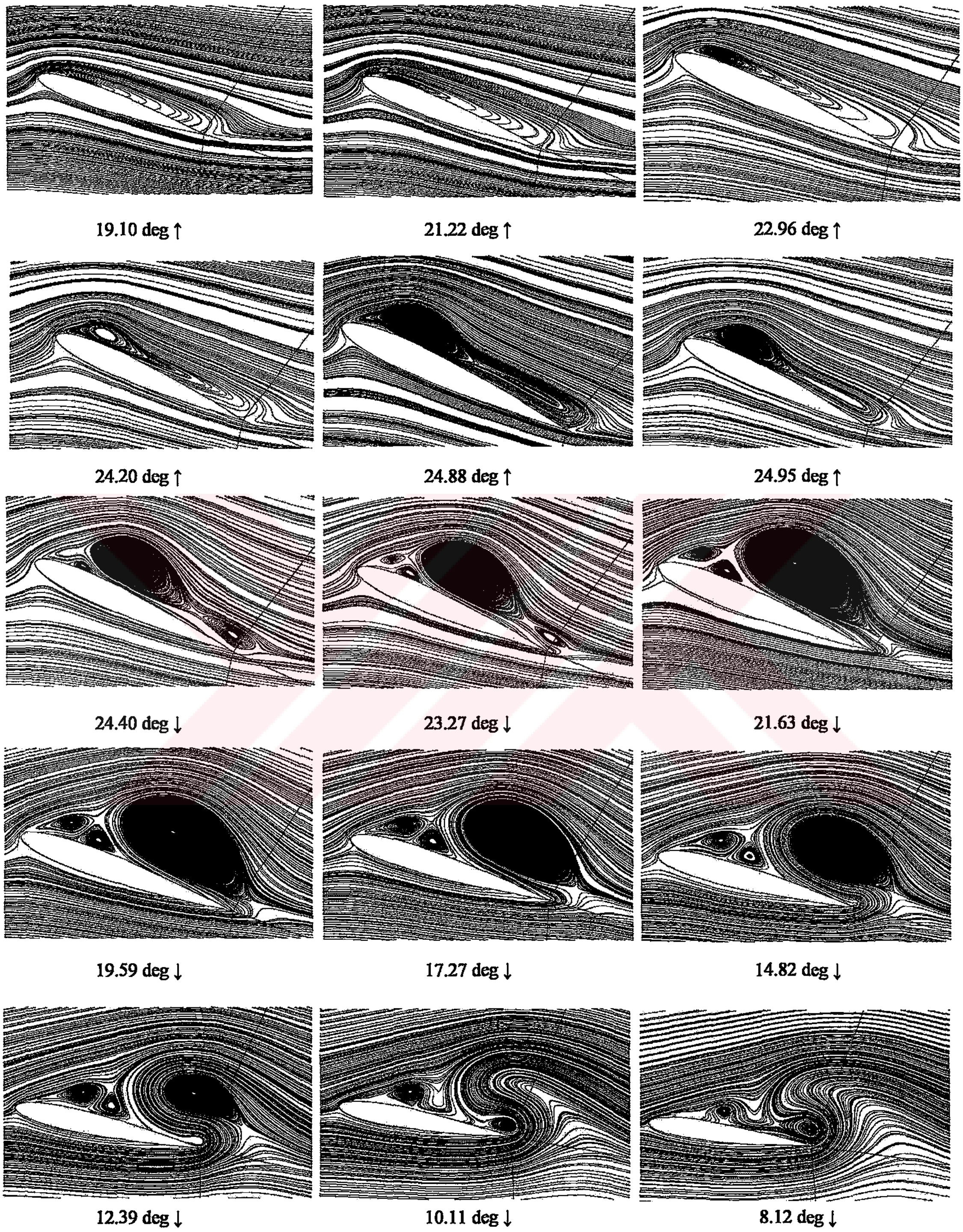

Figure 4.8: Streamline patterns at several angles of attack during upstroke (↑) and downstroke (↓) motions for a pitching NACA 0012 airfoil, at k = 0.50, $\alpha_0 = 10^\circ$, $\alpha_m = 15^\circ$, pitching axis at c/4, and $\mathrm{Re} = 10^4$.

In streamline patterns, it can be seen that the vortex structure in the same cycle is different during the upstroke and downstroke motions at the same incidences.

Group B: Reynolds number effects

In this group of simulations, Reynolds number is set at $Re = 3000$, which is (about three times) lower compared to that in group A. The amplitude and mean angle of attack are the same as before, $\alpha_0 = 10^\circ, \alpha_m = 15^\circ$, making $\alpha_{min} = 5^\circ$ and $\alpha_{max} = 25^\circ$. The values of reduced frequency are k = 0.15, 0.25 and 0.50 for cases 4, 5, and 6, respectively. As in all other cases, the normal force coefficients are plotted at reduced frequencies of k = 0.15, 0.25 and 0.50 in Figure 4.9, 4.10, and 4.11, respectively.

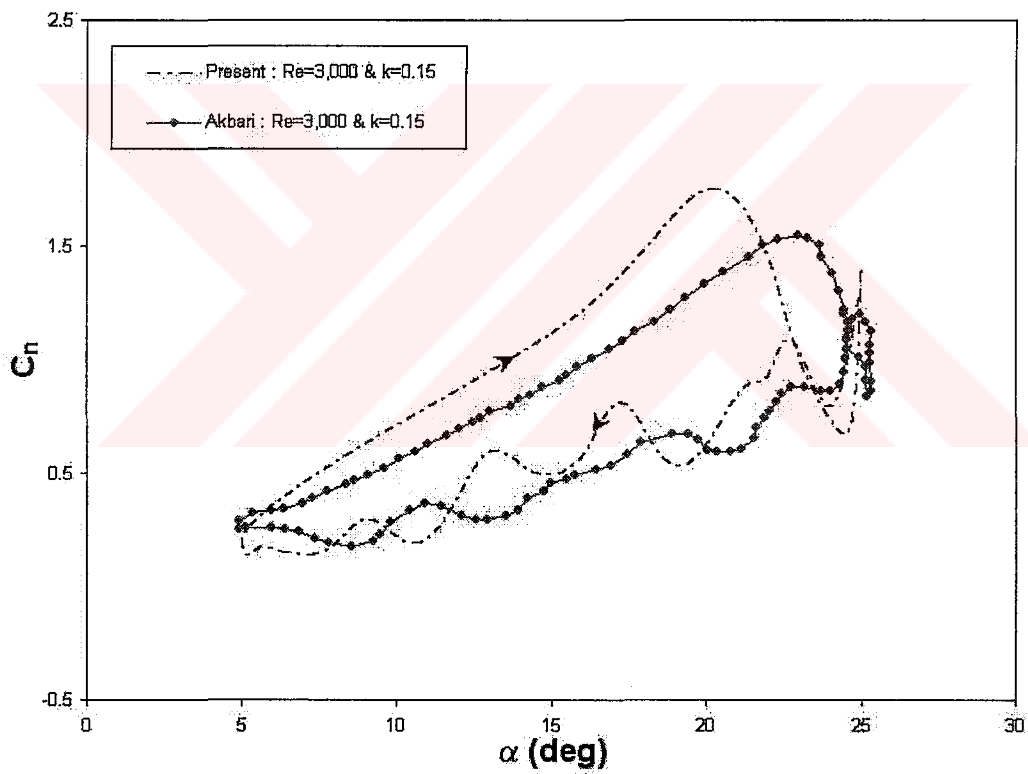

Figure 4.9: The hysteresis loop for normal force coefficient (Re = 3,000, k = 0.15).

Figure 4.2 should be compared to Figure 4.8 in order to investigate the effect of the Reynolds number on the dynamic stall at reduced frequency of $k = 0.15$. Results can be replotted as in Figure 4.12.

To investigate the effect of the Reynolds number on the dynamic stall at reduced frequency of k = 0.25, Figure 4.3 should be compared to Figure 4. Results can be replotted as below in Figure 4.13.

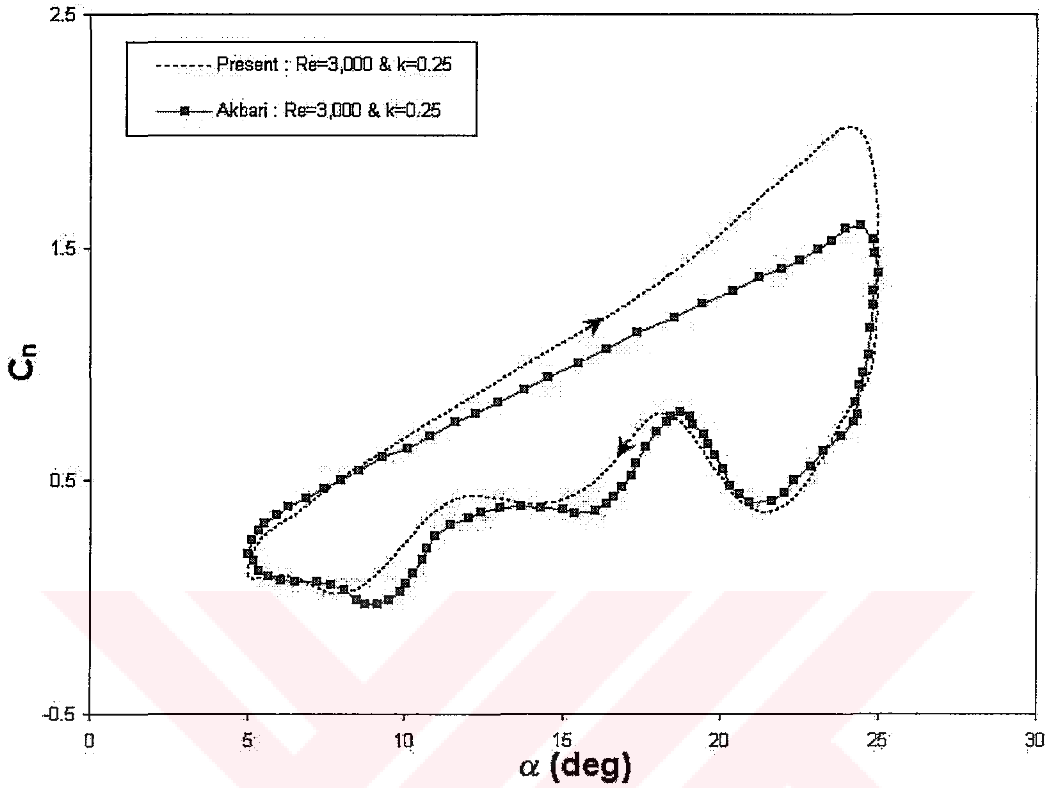

Figure 4.10: The hysteresis loop for normal force coefficient (Re = 3,000, k = 0.25).

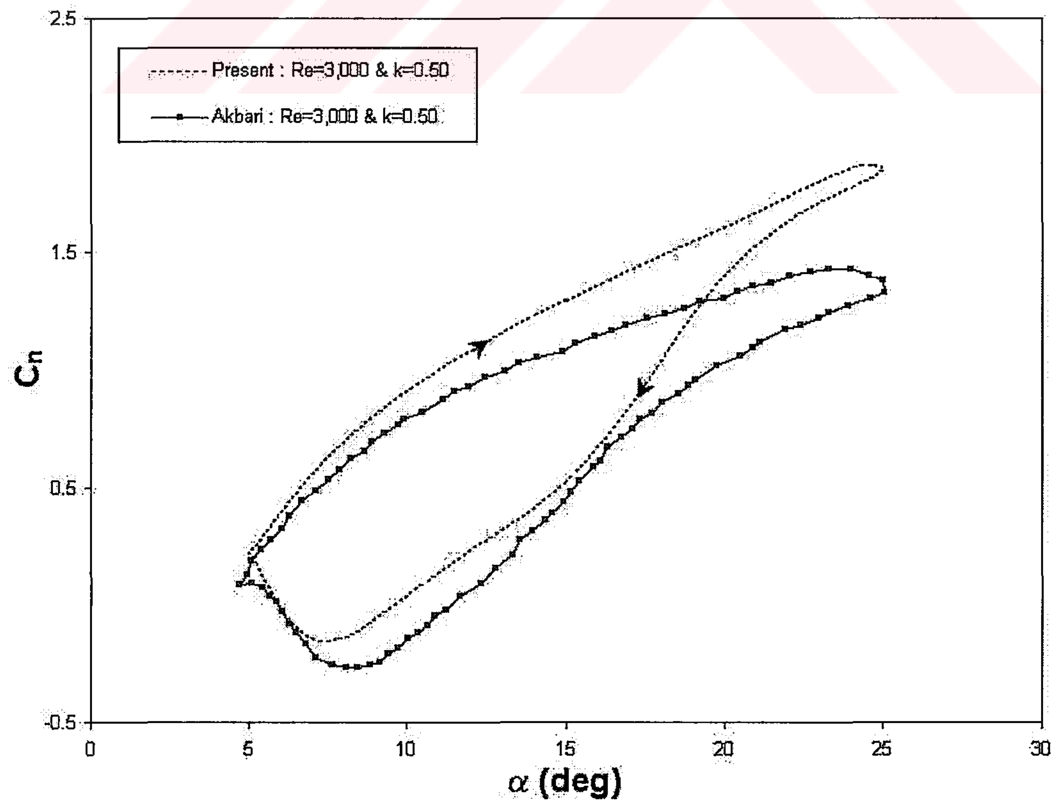

Figure 4.11: The hysteresis loop for normal force coefficient (Re = 3,000, k = 0.50).

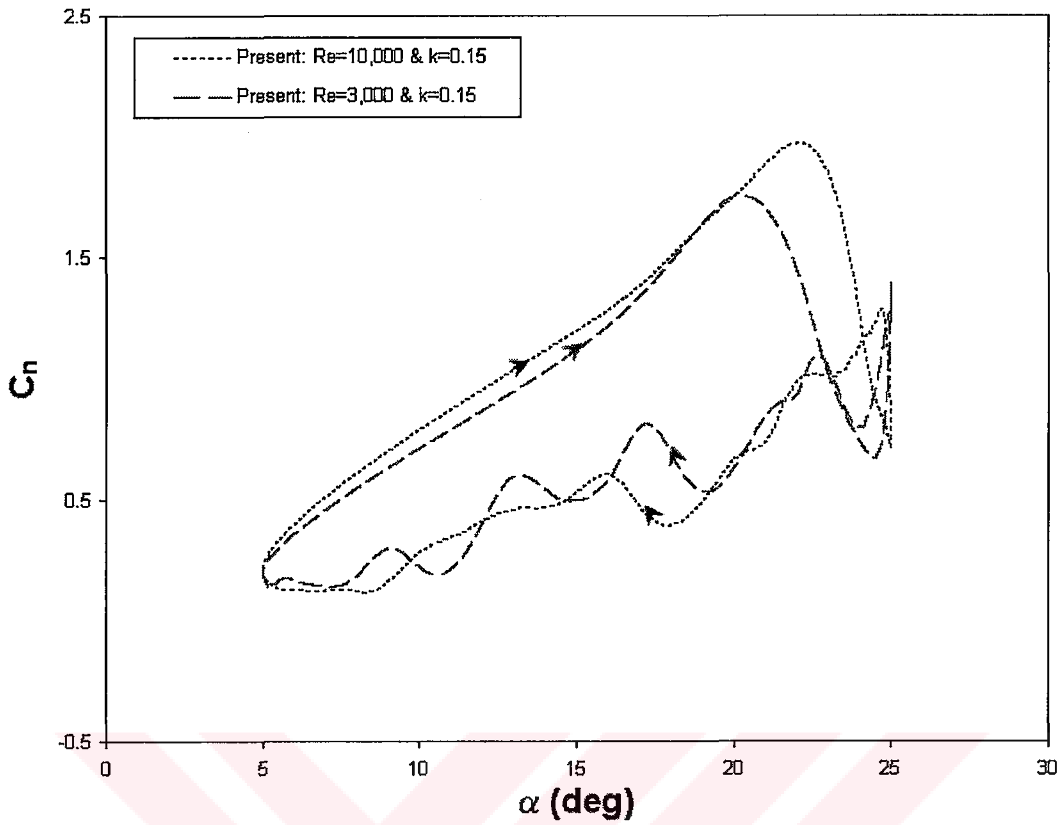

Figure 4.12: Comparison hysteresis loops for normal force coefficients at two different Reynolds numbers: Re =10,000 & 3,000 and k = 0.15.

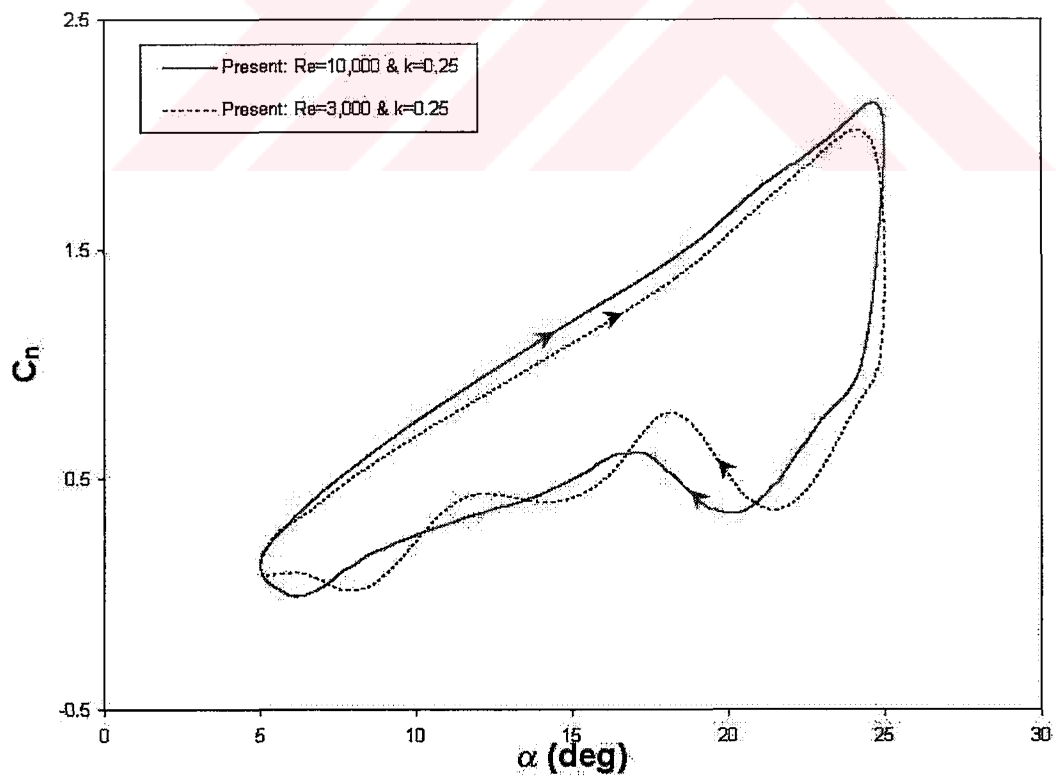

Figure 4.13: Comparison hysteresis loops for normal force coefficients at two different Reynolds numbers: Re = 10,000 & 3,000 and k = 0.25.

Figure 4.4 should be compared to Figure 4.10 in order to investigate the effect of the Reynolds number on the dynamic stall at reduced frequency of $k = 0.50$. Results can be replotted as below in Figure 4.14.

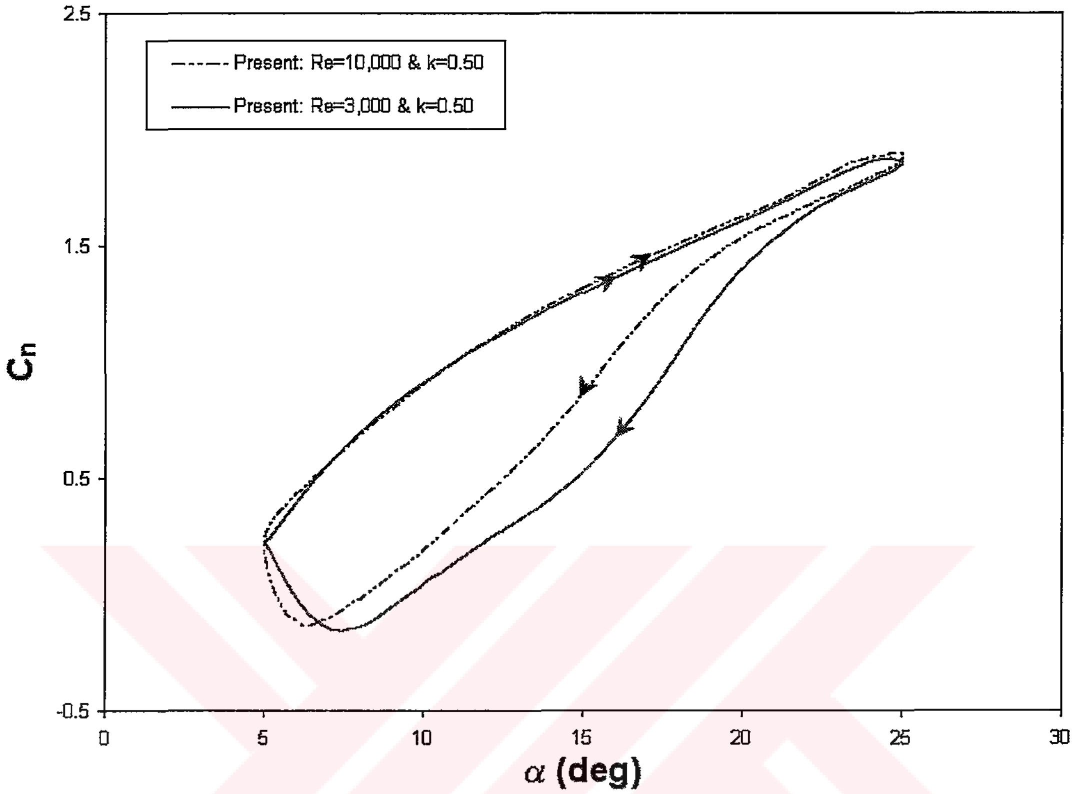

Figure 4.14: Comparison hysteresis loops for normal force coefficients at two different Reynolds numbers: Re = 10,000 & 3,000 and k = 0.50.

It is observed that, in general, the hysteresis loops in all corresponding cases in the two groups are very similar. Also, results show that the effect of Reynolds number to normal force coefficient is minimal. As the frequency increases these similarities become more obvious.

Group C: effects of mean angle of attack

In this group of simulations the mean incidence is increased to $\alpha_m = 20^\circ$, compared to other groups in which the mean incidence is at 15°. The amplitude of the pitching oscillation is kept at $\alpha_0 = 10^\circ$, making $\alpha_{\min} = 10^\circ$ and $\alpha_{\max} = 30^\circ$. The Reynolds number is set at $\mathrm{Re} = 10^4$, and the reduced frequency is set at k = 0.15, 0.25, and 0.50 in cases 7 to 9, respectively. The normal force coefficients are plotted in Figure 4.15, 4.16 and 4.17, for cases 7 to 9, respectively. These figures should be compared with

Figure 4.2, 4.3 and 4.4. As noted before, the only difference between groups A and C is in the mean incidence, which is 15° and 20° in these groups, respectively.

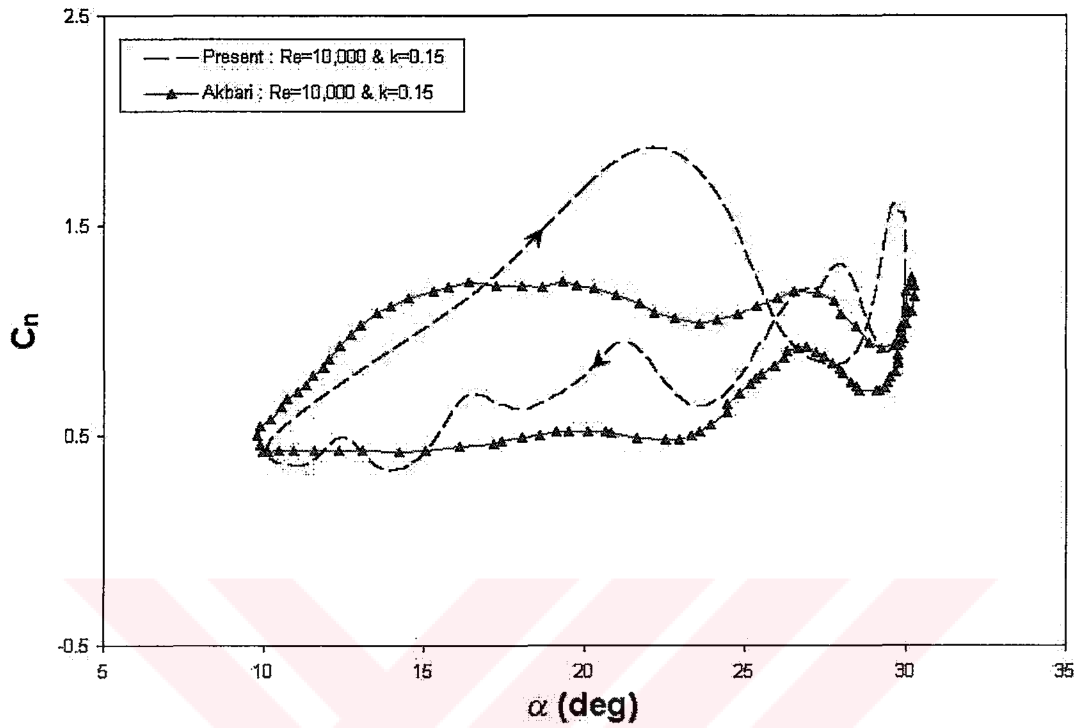

Figure 4.15: The hysteresis loop for normal force coefficient (Re = 10,000, k = 0.15)

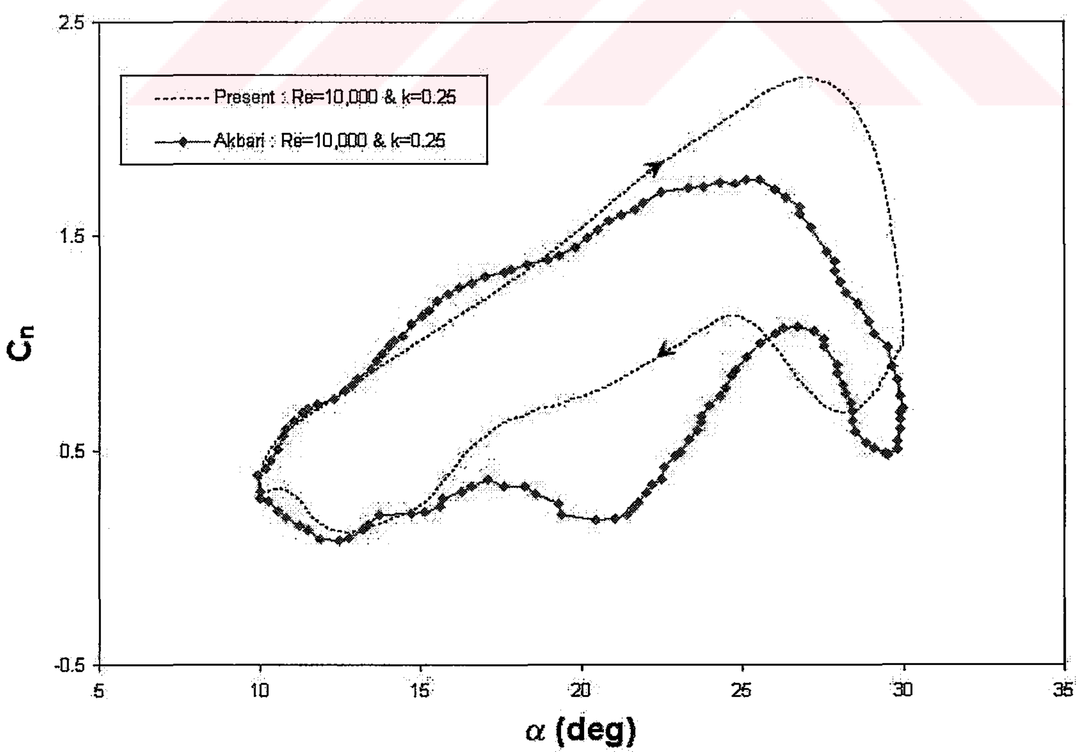

Figure 4.16: The hysteresis loop for normal force coefficient (Re = 10,000, k = 0.25)

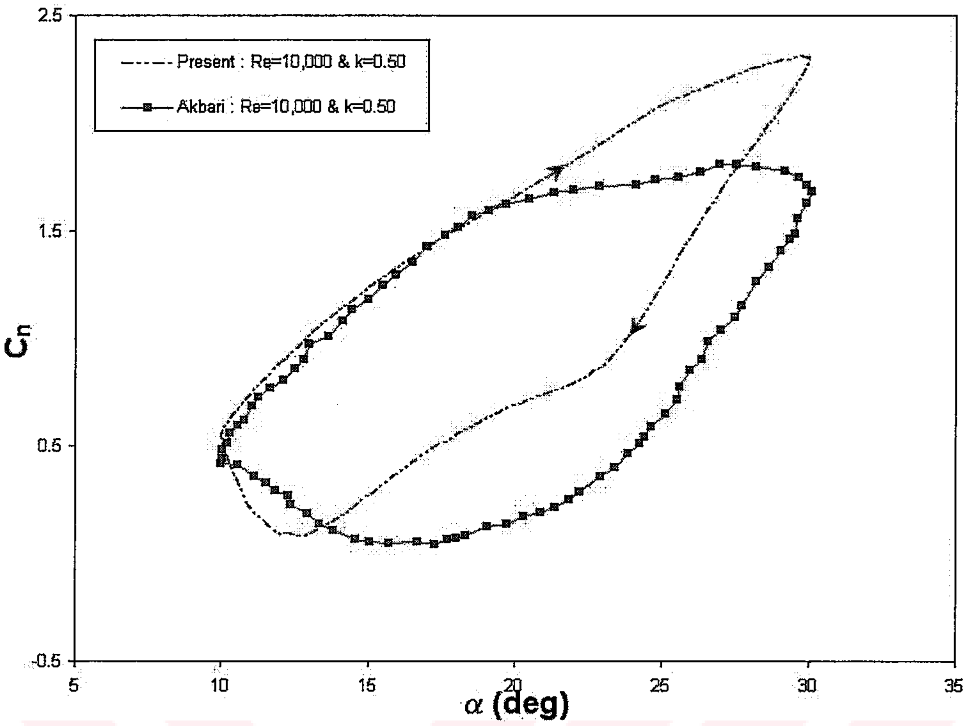

Figure 4.17: The hysteresis loop for normal force coefficient (Re = 10,000, k = 0.50)

The normal force coefficients obtained for these analyses are plotted together with the results of the corresponding case from group A (i.e. same Re number and reduced frequency but different mean incidence) in Figure 4.18, 4.19 and 4.20 for the reduced frequency values of k = 0.15, 0.25 and 0.50, respectively.

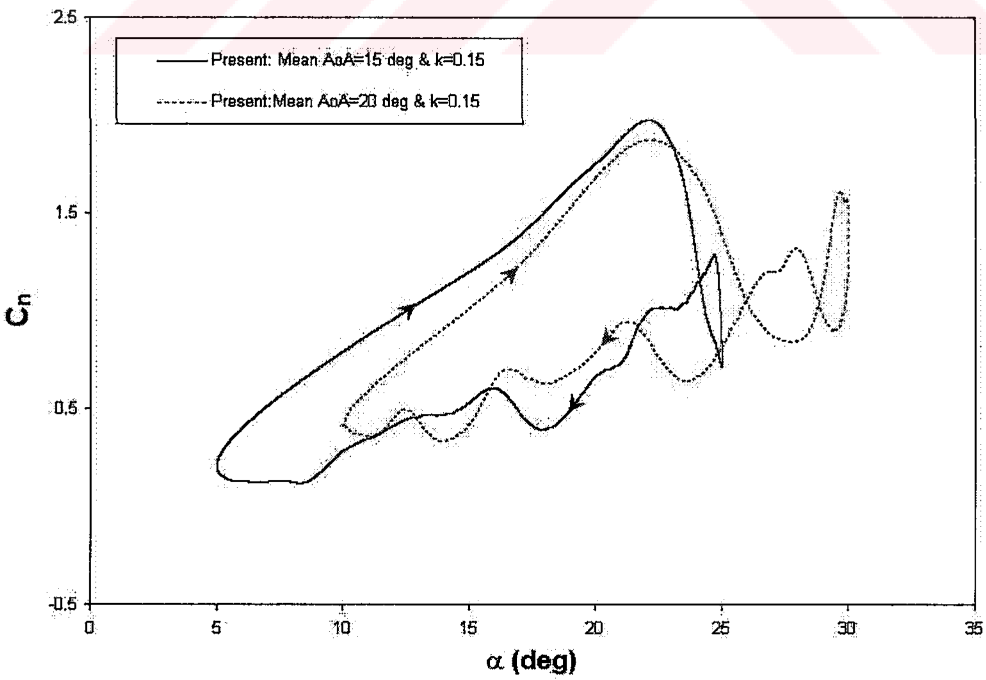

Figure 4.18: Comparison hysteresis loops for normal force coefficients at two different mean incidences: $\alpha_m = 15^{\circ}$ and $\alpha_m = 20^{\circ}$, k = 0.15.

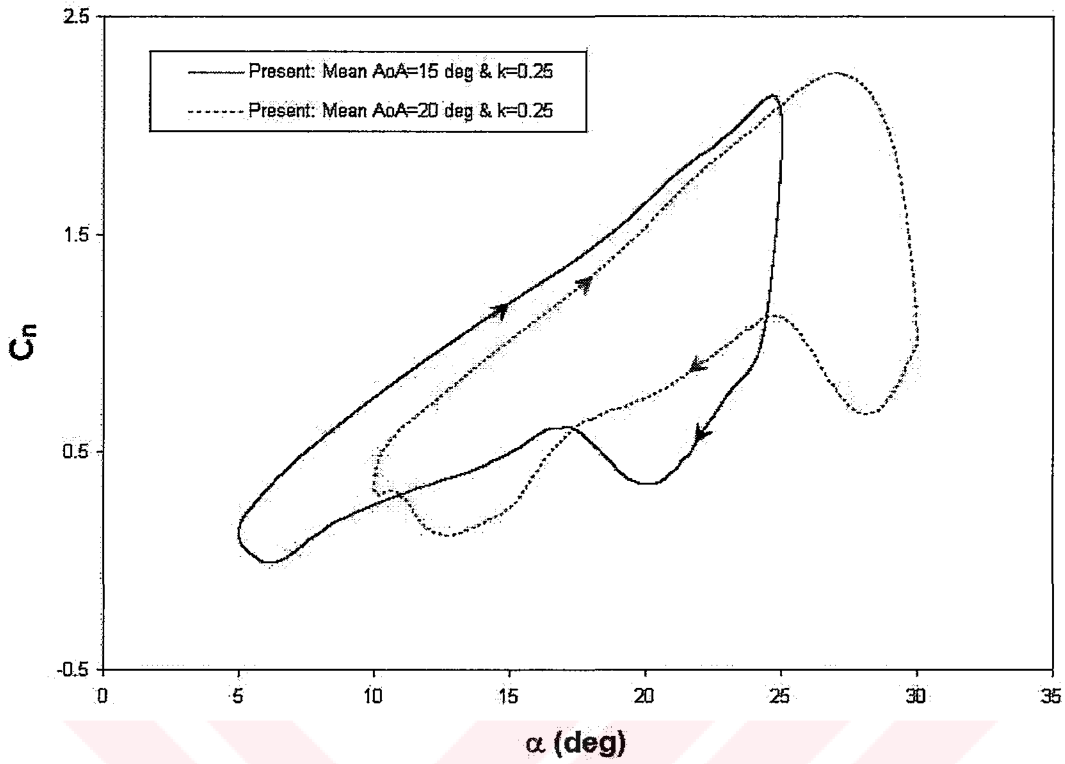

Figure 4.19: Comparison hysteresis loops for normal force coefficients at two different mean incidences: $\alpha_m = 15^\circ$ and $\alpha_m = 20^\circ$, k = 0.25.

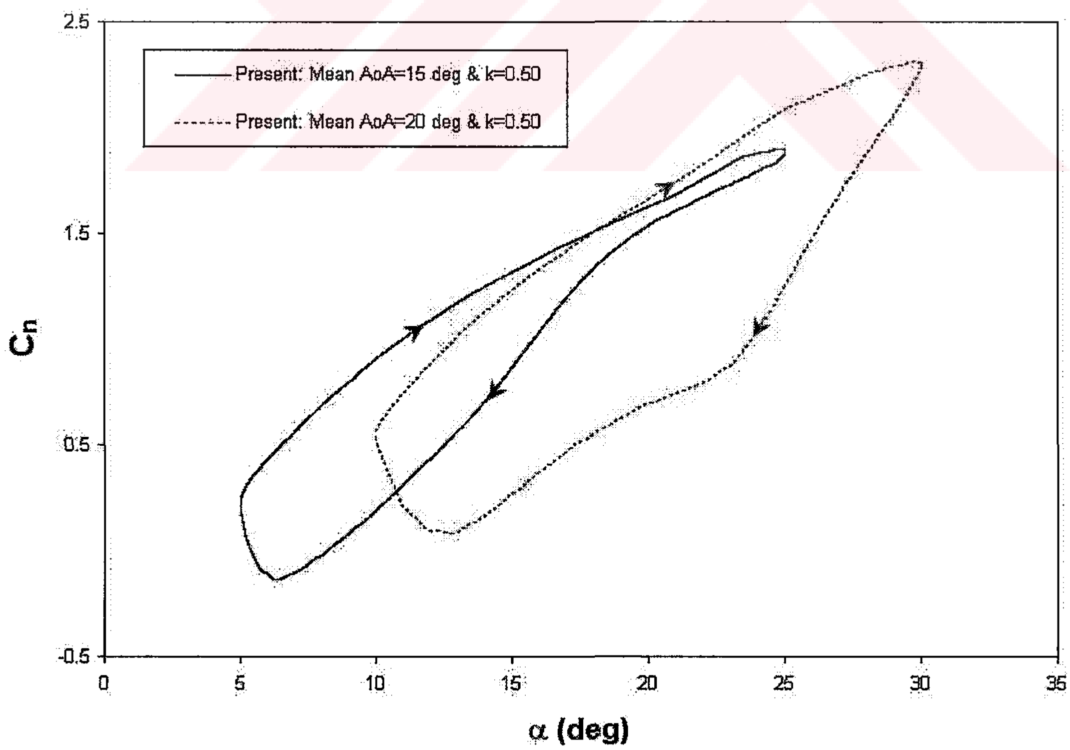

Figure 4.20: Comparison hysteresis loops for normal force coefficients at two different mean incidences: $\alpha_m = 15^\circ$ and $\alpha_m = 20^\circ$, k = 0.50.

The results show that the difference of mean incidence between groups A and C, yields results which are very similar in trend but slightly shifted to give higher maximum force coefficient. Also, it can be concluded that an increase in the mean incidence has some considerable effects on the normal force coefficient of a pitching airfoil: the hysteresis loops become wider, both the maximum value and the average of the force coefficients increase. Furthermore, stall may occur at lower frequencies of oscillation, due to an increase in the incidence.

4.3. Dynamic Stall in Turbulent Flow Conditions

In this section, results obtained from our turbulent flow simulation cases over a pitching NACA 0015 airfoil are presented. In all computations of this section, $k-\varepsilon$ turbulence model with wall function is used to predict fully turbulent flow conditions over a NACA 0015 pitching airfoil.

Three pitching airfoil cases are selected to simulate no stall, stall onset, and deep stall regimes at Re = $2\text{x}10^6$ and M = 0.3. A summary of the case-studies for a pitching NACA 0015 airfoil in turbulent flow conditions is presented in Table 4.2. Our results will be compared with experimental data performed by Piziali [19]. All computations of pitching NACA 0015 airfoil are initiated as fully turbulent flow conditions because the flow was tripped at the leading edge to ensure a fully turbulent flow in the experiment.

Table 4.2: List of turbulent flow simulation cases.

CASE	Reynolds Number, Re	Mean angle of attack, α_m(deg)	Amplitude of oscillation, α_0(deg)	Reduced frequency, k	Pitch axis location
No stall	$2\text{x}10^6$	4	2	0.038	c/4
Stall Onset	$2\text{x}10^6$	11	2	0.038	c/4
Deep Stall	$2\text{x}10^6$	13	5	0.038	c/4

First of all, some grid sensitivity studies are performed in stationary airfoil cases to reach the most suitable computational grid in the fully turbulent flow conditions (see Figure 4.21). Four different grids in the number of grid points and distribution of the grid points are generated by CFD-GEOM. All meshes consist of two blocks, around airfoil and at wake region. Mesh I has 138x39 cells around airfoil and 78x49 cells at wake, and $3x10^{-3}c$ initial wall spacing. There are 138x59 cells around airfoil and 118x49 cells at wake region in mesh II. Also, it has $3.1x10^{-3}c$ initial wall spacing. Mesh IV consists of 200x100 cells around airfoil and 200x40 cells at wake, and it has $2x10^{-2}c$ initial wall spacing.

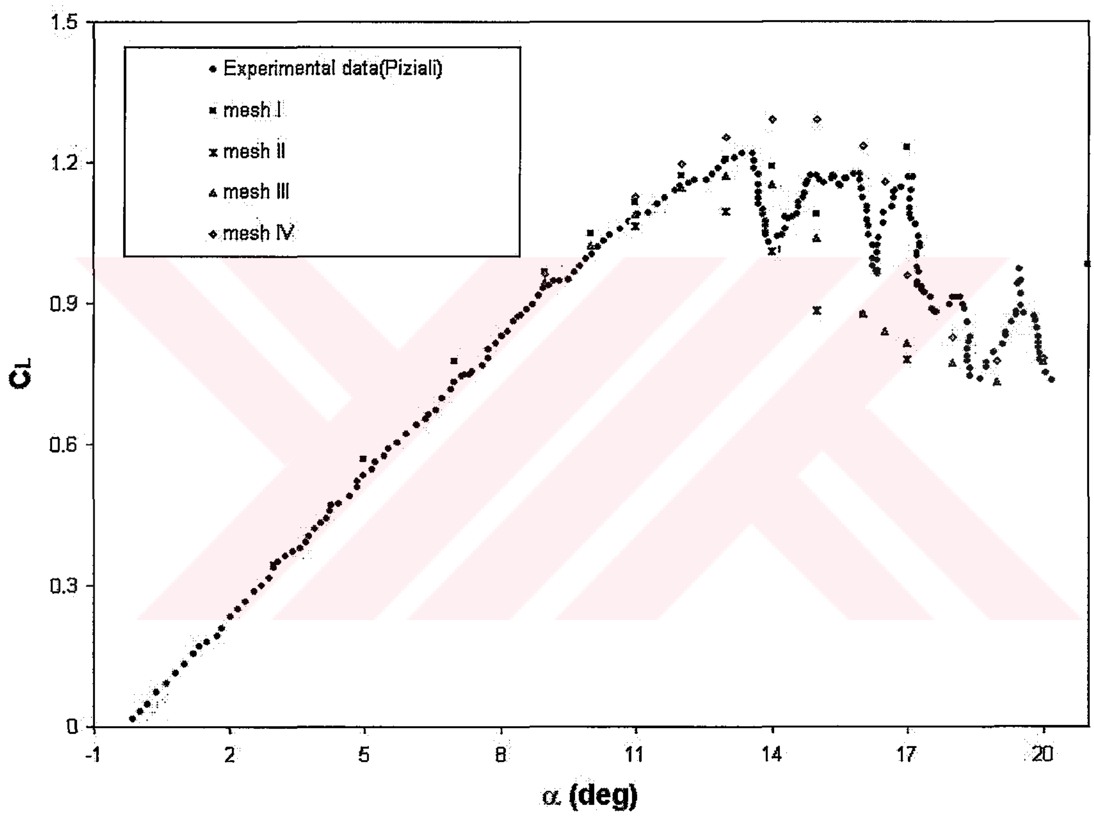

Figure 4.21: Quasi-steady studies for stationary airfoil case in fully turbulent flows.

It can be seen from the figure that mesh III is the most suitable mesh for turbulent flow computations because it can predict the approximately the same separation angle according to experimental data. Mesh III consists of two blocks, first is around the airfoil with 138x59 cells and second is in the wake region with 118x49 cells. As it can be seen in Figure 4.22, farfield boundary is extended 10 chord lengths from surface. The airfoil chord length is about 0.3048 m (1 ft) and the initial wall spacing is $3x10^{-3}c$.

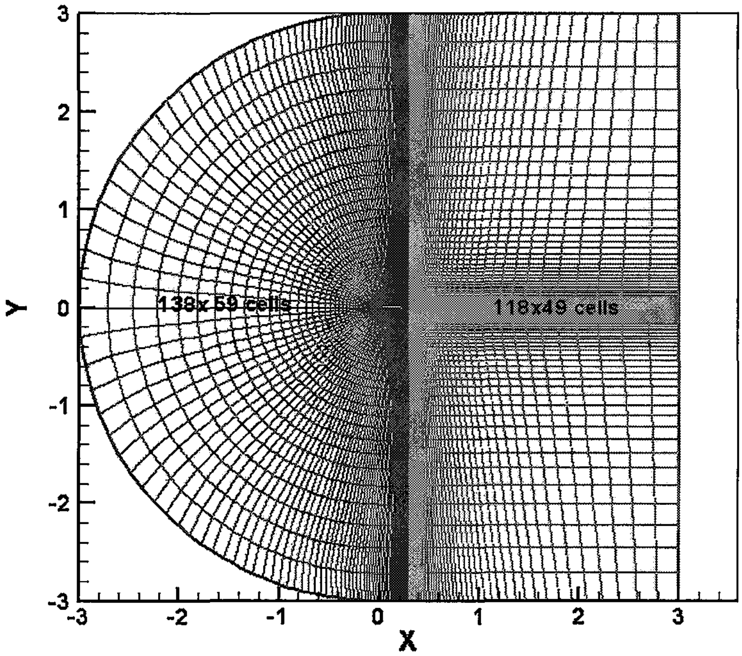

Figure 4.22: Computational domain in fully turbulent flow conditions (mesh III).

Attached flow simulation is performed at $\alpha_m = 4^\circ$ and $\alpha_0 = 2^\circ$. NACA 0015 airfoil pitches about the quarter-chord between $\alpha_{\min} = 2^\circ$ and $\alpha_{\max} = 6^\circ$. A steady-state solution is obtained at the mean incidence $\alpha_m = 4^\circ$, using free stream conditions as initial solution. Then, the converged solution is used as an initial condition for the unsteady computations. The unsteady periodic solution is obtained after three cycles. The lift coefficient for this case is plotted in Figure 4.23.

Stall onset regime is simulated at of $\alpha_m = 11^\circ$ and $\alpha_0 = 2^\circ$. The airfoil pitches about again the quarter-chord between $\alpha_{\min} = 9^\circ$ and $\alpha_{\max} = 13^\circ$. A steady-state solution is obtained at the mean incidence $\alpha_m = 11^\circ$, using free stream conditions as initial solution. Then, the converged solution is used as an initial condition for the unsteady computations. The lift coefficient versus angle of attack for this case is plotted in Figure 4.24.

Deep stall regime is simulated at $\alpha_m = 13^\circ$ and $\alpha_0 = 5^\circ$. NACA 0015 airfoil pitches about the quarter-chord between $\alpha_{\min} = 8^\circ$ and $\alpha_{\max} = 18^\circ$. A steady-state solution is obtained at the mean incidence $\alpha_m = 13^\circ$, using free stream conditions as initial solution. The unsteady periodic solution is obtained after three cycles. Results of mesh III and mesh IV are plotted as a lift coefficient for this case in Figure 4.25 and Figure 4.26, respectively.

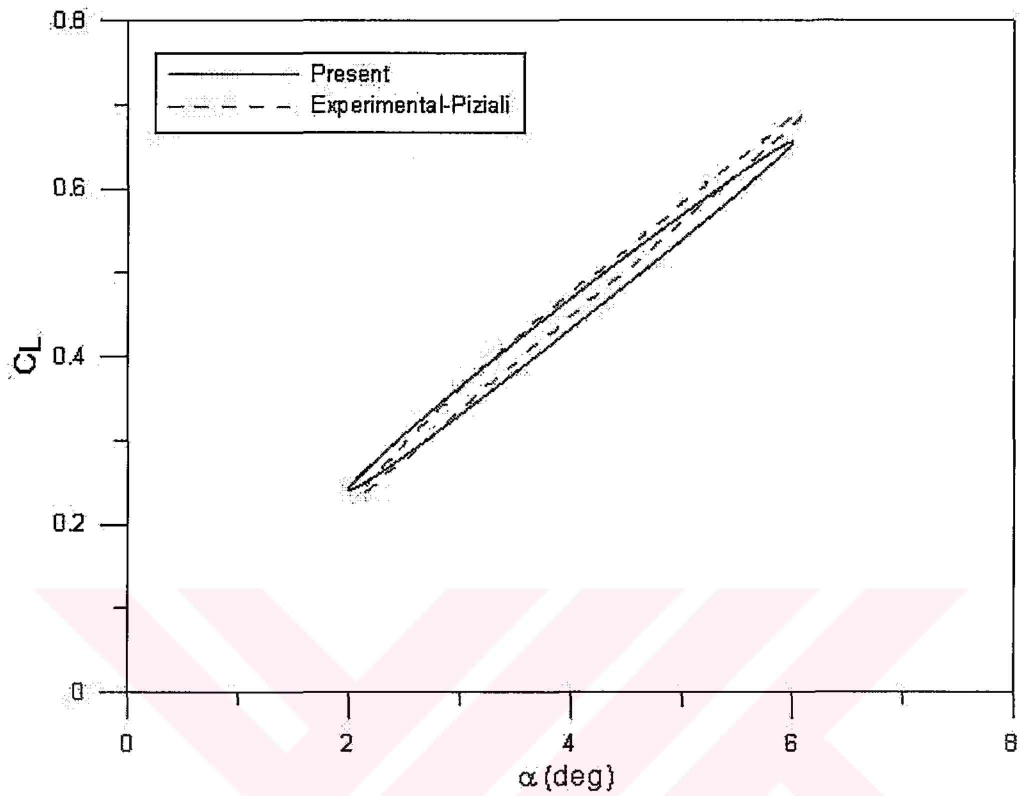

Figure 4.23: Lift coefficient during the no stall regime ($\alpha_m = 4^\circ, \alpha_0 = 2^\circ$).

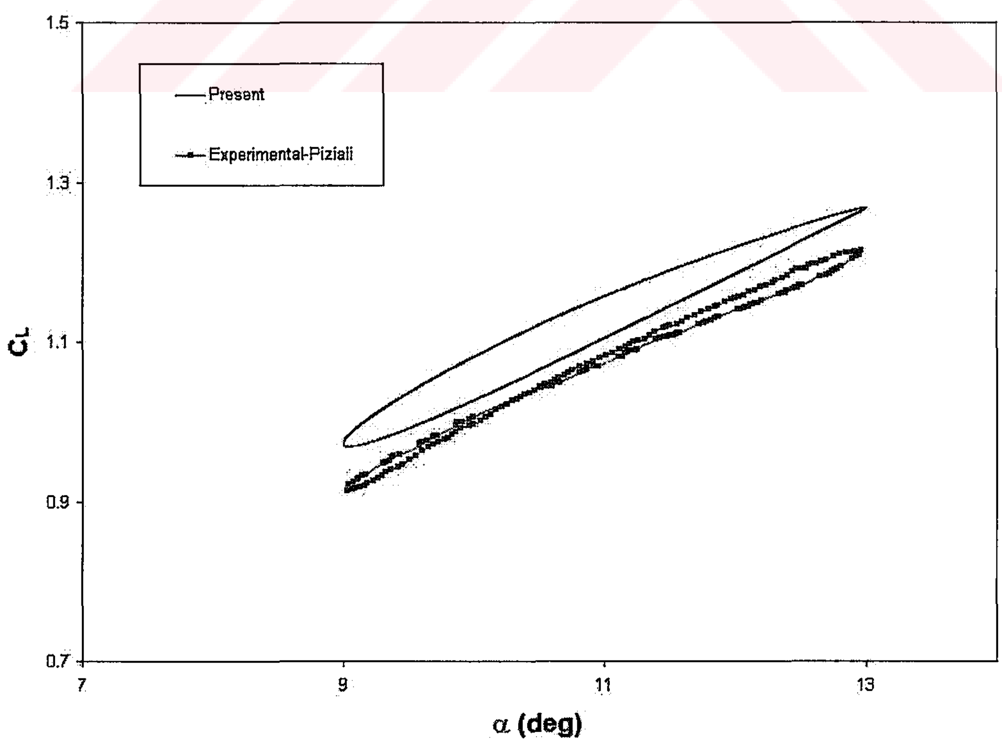

Figure 4.24: Lift coefficient during the stall onset regime ($\alpha_m = 11^\circ, \alpha_0 = 2^\circ$).

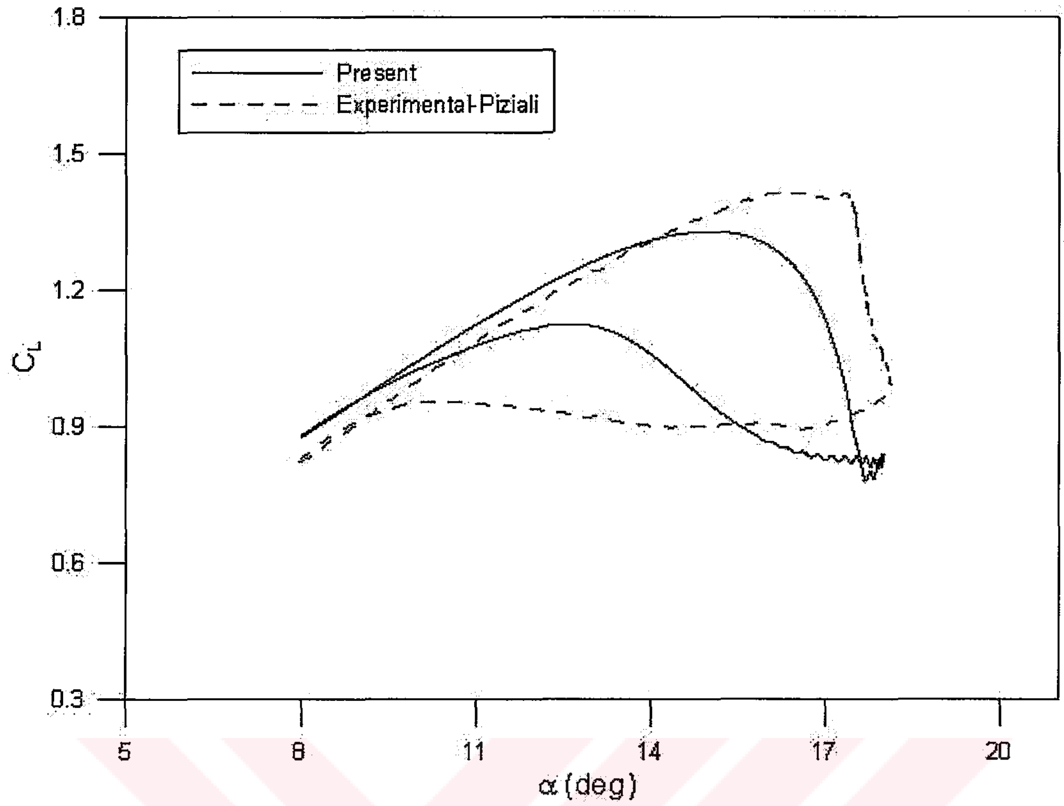

Figure 4.25: C_L vs. α during the deep stall regime by mesh III ($\alpha_m = 13^\circ$, $\alpha_0 = 5^\circ$).

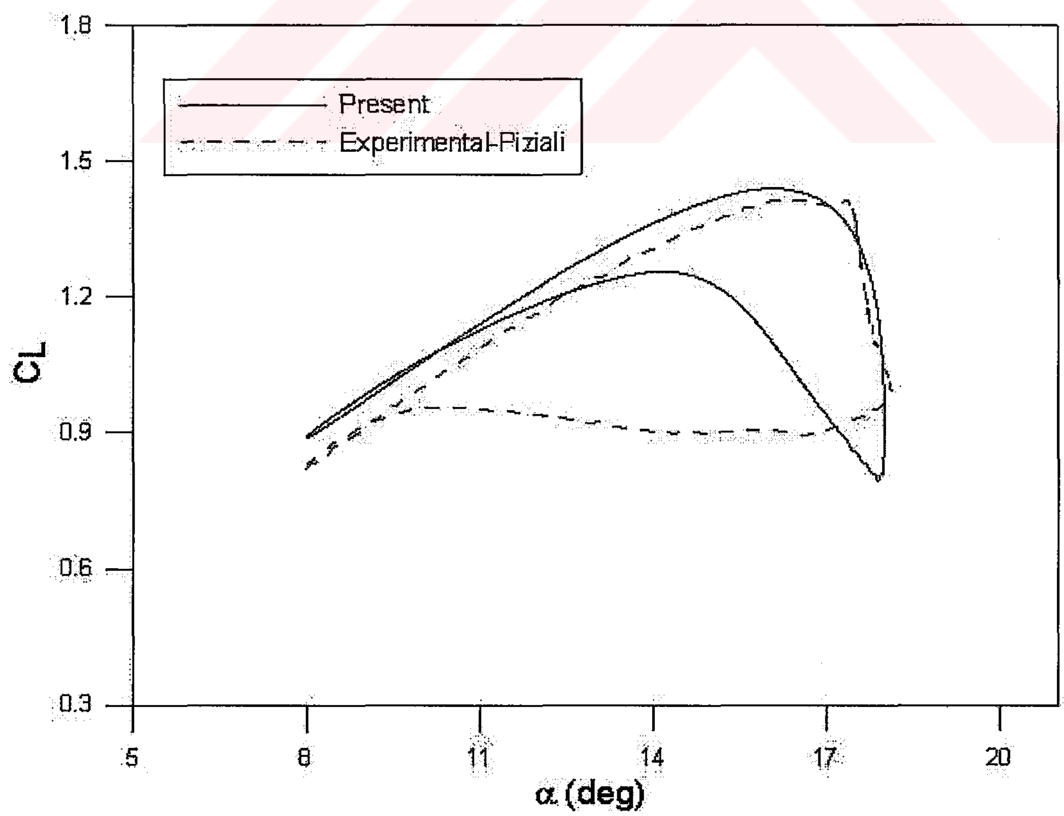

Figure 4.26: C_L vs. α during the deep stall regime by mesh IV ($\alpha_m = 13^\circ$, $\alpha_0 = 5^\circ$).

Streamline patterns at several incidences during the upstroke and downstroke at reduced frequency of k = 0.038 and $\alpha_m = 13^\circ$, $\alpha_0 = 5^\circ$ are shown in Figure 4.27.

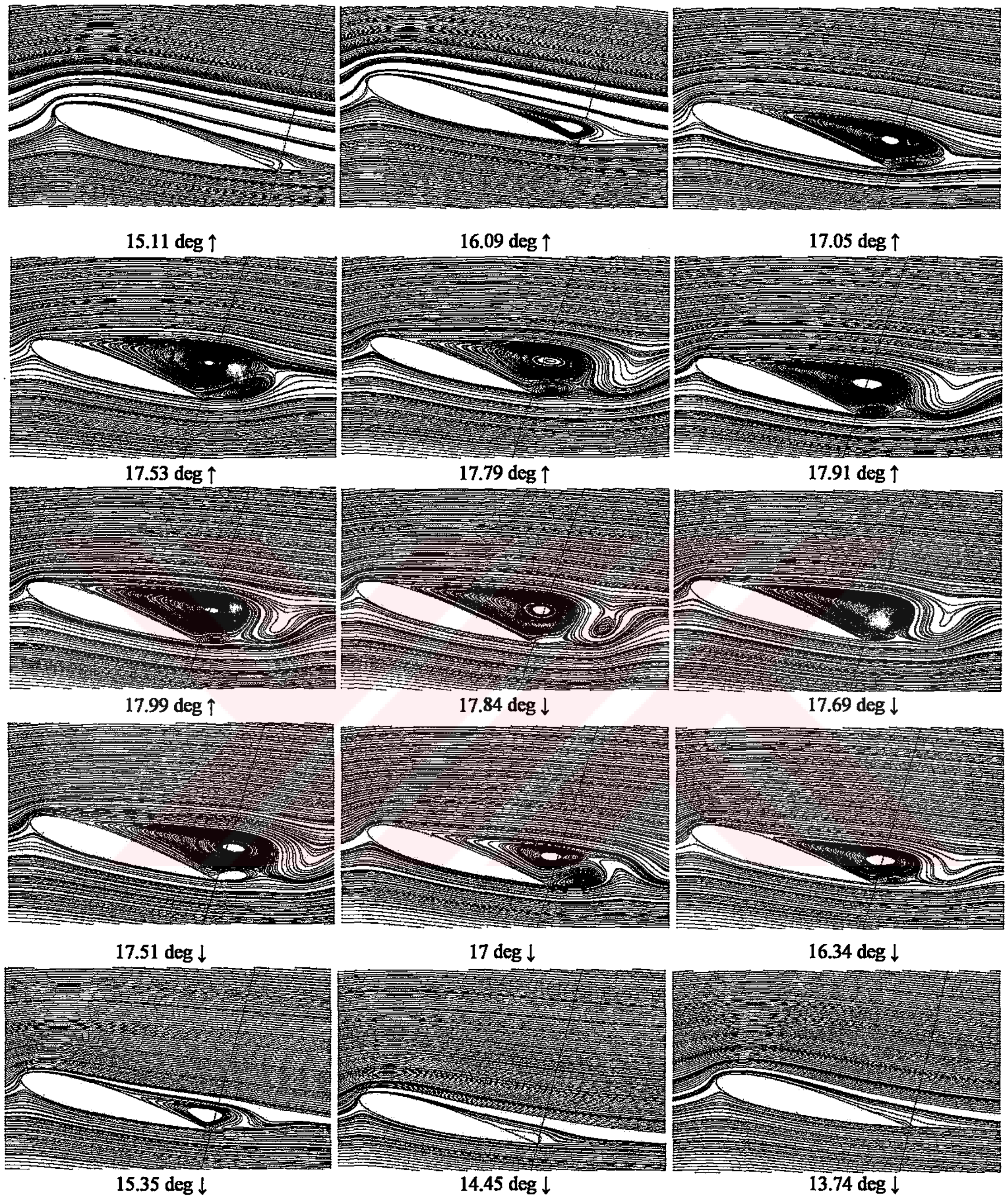

Figure 4.27: Streamline patterns at several angles of attack during upstroke (↑) and downstroke (↓) motions for a pitching NACA 0015 airfoil, at k = 0.038($\alpha_m = 13^\circ$, $\alpha_0 = 5^\circ$)

5. CONCLUSIONS AND FUTURE RESEARCH

A commercial CFD code is used to compute the flow field around pitching airfoils. The structured C-grids are generated to simulate flow field. Considered case-studies in this study consist of pitching NACA 0012 airfoil cases in laminar flow conditions and pitching NACA 0015 airfoil cases in turbulent flow conditions. The flow field around pitching airfoils is simulated by solving viscous Navier- Stokes equations in a Finite Volume discretization scheme with MUSCL approach.

As the dynamic stall behavior is of primary interest, the effects of the reduced frequency, mean incidence and Reynolds number on the dynamic stall characteristics of the airfoil, in term of the normal force coefficient, as well as the flow field structure, were investigated in the laminar flow simulation part of the present study. It was observed that pitching oscillations of the airfoil delayed the flow separation to higher incidences compared to a steady stall angle. The normal force was observed to increase well beyond that at the steady stall angle. The separation was observed to start from the leading-edge, followed by the formation and convection of a vortex along the suction surface of the airfoil. Trailing edge vortices were also observed to form and shed from the airfoil, following the leading-edge vortex. During the downstroke, one or more secondary vortices were observed to form and release from the suction surface, after the release of the primary dynamic stall vortex. Our laminar simulation results for the dynamic stall flow of the airfoil were compared against available numerical data [40], and good agreements were obtained.

The reduced frequency of oscillation was found to have major effect on the flow field and on the normal force coefficient of the airfoil. The flow separation was observed to delay up to higher incidences with increasing reduced frequency. Hence, the maximum normal force coefficient occurred at higher angles of attack by increasing the reduced frequency. The Reynolds number, on the other hand, was found to have little effect on the dynamic stall characteristics of the airfoil, in the range of Re = 3,000 to 10,000 considered in our simulations. Increasing the mean incidence caused flow separation to occur earlier in an oscillation cycle, even lower angles of attack compared to a case with only a lower mean incidence. Also, hysteresis effects in the force coefficient loop intensified and the maximum normal force coefficient increased.

In all turbulent flow calculations, $k-\varepsilon$ turbulence model with wall function is used to predict fully turbulent flow conditions over a pitching airfoil. Three pitching airfoil cases are selected to simulate no stall, stall onset, and deep stall regimes. The $k-\varepsilon$ turbulence model gave good predictions for the attached and stall onset cases, and moderate predictions for deep stall case. For deep stall case, it was found that it is important to model the leading edge transional flow behaviour in order to obtain the experimentally observed results.

The problem of dynamic stall has been encountered in various aerodynamic applications, including aircraft manoeuvrability, helicopter rotors, wind turbines, turbomachinery blades and even insect and unmanned air vehicle (UAV) wings. Successful control and delay of the dynamic stall may significantly improve the performance in all of these aerodynamic applications. A number of techniques, such as geometrical modifications to the airfoil, periodic excitation through surface vibrations, plasma actuation, leading edge suction and synthetic jets are proposed for dynamic stall. One of the most promising tools is the synthetic jet actuator (SJA). No detailed study, however, is available on the effect of synthetic jets on dynamic stall over pitching airfoils. The effect of SJA on the controlling of dynamic stall will be our future work.

REFERENCES

[1] **Harris, F.D. and Pruyn, R.R.**, 1968. Blade Stall-Half Fact, Half Fiction, *Journal of the American Helicopter Society*, **13**, 27-48.

[2] **Ham, N.D. and Garelick, M.S.**, 1968. Dynamic Stall Considerations in Helicopter Rotors, *Journal of the American Helicopter Society*, **13**, 49-55.

[3] **Gustafson, F.B. and Myers, G.C.**, 1946. Stalling of Helicopter Blades, NACA Report No.840.

[4] **Ham, N.D.**, 1968. Aerodynamic Loading on a Two-Dimensional Airfoil During Dynamic Stall, *AIAA Journal*, **6**, 1927-1934.

[5] **Liiva, J.**, 1969. Unsteady Aerodynamic and Stall Effects on Helicopter Rotor Blade Airfoil Sections, *AIAA Journal,* **6**, 46-51.

[6] **McCroskey, W.J., Carr, L.W. and McAlister, K.W.**, 1976. Dynamic Stall Experiments on Oscillating Airfoils, *AIAA Journal*, **14,** 57-63.

[7] **McAlister, K.W., Carr, L.W. and McCroskey, W.J.**, 1978. Dynamic Stall Experiments on the NACA 0012 Airfoil, NASA TP-1100, NASA Ames Research Center, Moffet Field, CA.

[8] **McAlister, K.W. and Carr, L.W.**, 1979. Water Tunnel Visualizations of Dynamic Stall, *Transactions of the ASME, Journal of Fluid Engineering*, **101**, 376-380.

[9] **Walker, J.M., Helin, H.E. and Strickland, J.H.**, 1985. An Experimental Investigation of an Airfoil Undergoing Large-Amplitude Pitching Motions, *AIAA Journal*, **23,** 1141-1142.

[10] **Lorber, P.F. and Carta, F.O.**, 1988. Airfoil Dynamic Stall at Constant Pitch Rate and High Reynolds Number, *Journal of Aircraft*, **25**, 548-556.

[11] **Chandrasekhara, M.S. and Brydges, B.E.**, 1990. Amplitude Effects on Dynamic Stall of an Oscillating Airfoil, AIAA Paper 90-0575, 28th Aerospace Sciences Meeting, Reno, NV.

[12] **Shih, C., Lourenco, L., Dommelen, L.V. and Krothapalli, A.**, 1992. Unsteady Flow Past an Airfoil Pitching at a Constant Rate, *AIAA Journal*, **30**, 1153-1161.

[13] **Schreck, S.J., Faller, W.E. and Helin, H.E.**, 1998. Pitch Rate and Reynolds Number Effects on Unsteady Boundary-Layer Transition and

Separation, *Journal of Aircraft*, **35**, 46-52.

[14] **Chandrasekhara, M.S. and Carr, L.W.**, 1990. Flow Visualization Studies of the Mach Number Effects on Dynamic Stall of an Oscillating Airfoil, *Journal of Aircraft*, **27**, 516-522.

[15] **Chandrasekhara, M.S., Ahmed, S. And Carr, L.W.**, 1993. Schlieren Studies of Compresibbility Effects on Dynamic Stall of Transiently Pitching Airfoils, *Journal of Aircraft*, **30**, 213-220.

[16] **Carr, L.W. and Chandrasekhara, M.S.**, 1996. Compresibility Effects on Dynamic Stall, *Prog. Aerospace Sci.*, **32**, 523-573.

[17] **Raffel, M., Kompenhans, J. and Wernert, P.**, 1995. Investigation of the Unsteady Flow Velocity Field Above an Airfoil Pitching Under Deep Dynamic Stall Conditions, *Experiments in Fluids*, **19**, 103-111.

[18] **Wernet, P., Koerber, G., Wietrich, F. et al.**, 1997. Demonstration by PIV of Non-Reproducibility of the Flow Field Around an Airfoil Pitching Under Deep Dynamic Stall Conditions and Consequences Thereof, *Aerospace Science and Technology*, **2**, 125-135.

[19] **Piziali, R.A.**, 1994. An Experimental Investigation of 2-D and 3-D Oscillating Wing Aerodynamics For a Range of Angles of Attack Including Stall, NASA TM-4632, NASA Ames Research Center, Moffett Field, CA.

[20] **Ericsson, L.E. and Reding J.P.**, 1971b. Unsteady Airfoil Stall, Review and Extension, *Journal of Aircraft*, **8**, 609-616.

[21] **Ericsson, L.E. and Reding J.P.**, 1972. Dynamic Stall of Helicopter Blades, *Journal of the American Helicopter Society*, **17**, 11-19.

[22] **Ericsson, L.E. and Reding J.P.**, 1980. Dynamic Stall at High Frequency and Large Amplitude, *Journal of Aircraft*, **8**, 579-583.

[23] **Ericsson, L.E. and Reding J.P.**, 1988a. Fluid Mechanics of Dynamic Stall Part I. Unsteady Flow Concepts, *Journal of Fluids and Structures*, **2**, 1-33.

[24] **Ericsson, L.E. and Reding J.P.**, 1988b. Fluid Mechanics of Dynamic Stall Part II. Prediction of Full Scale Characteristics, *Journal of Fluids and Structures*, **2**, 113-143.

[25] **Mehta, U.B.**, 1977. Dynamic Stall of an Oscillating Airfoil, AGARD CP-227, Paper No.23, 1-32.

[26] **Sankar, N.L. and Tassa, Y.**, 1981. Compresibility Effects on Dynamic Stall of an NACA 0012 Airfoil, *AIAA Journal*, **19**, 557-558.

[27] **Visbal, M.R. and Shang, J.S.**, 1989. Investigation of the Flow Structure Around a Rapidly Pitching Airfoil, *AIAA Journal*, **27**,1044-1051.

[28] **Guo, W.H., Fu, D.X. and Ma, Y.W.**, 1994. Numerical Investigation of Dynamic Stall of an Oscillating Aerofoil, *International Journal for Numerical Methods in Fluids*, **19**, 723-734.

[29] **Akbari, M.H. and Price, S.J.**, 2003. Simulation od Dynamic Stall for a NACA 0012 Airfoil Using a Vortex Method, *Journal of Fluids and Structures*, **17**, 855-874.

[30] **Tuncer, I.H., Wu, J.C. and Wang, C.M.**, 1990. Theoretical and Numerical Studies of Oscillating Airfoils, *AIAA Journal*, **28**, 1615-1624.

[31] **Ekaterinaris, J.A.**, 1989. Compressible Studies on Dynamic Stall, AIAA Paper 89-0024.

[32] **Fung, K.Y. and Carr, L.W.**, 1991. Effects of Compresibility on Dynamic Stall, *AIAA Journal*, **26**, 306-308.

[33] **Currier, J.M. and Fung, K.-Y.**, 1992. Analysis of the Onset of Dynamic Stall, *AIAA Journal*, **30**, 2469-2477.

[34] **Rizzetta, D.P. and Visbal, M.R.**, 1992. Comparative Numerical Study of Two Turbulence Models for Airfoil Static and Dynamic Stall, *AIAA Journal*, **31**, 784-786.

[35] **Ekaterinaris, J.A. and Menter, F.R.**, 1994. Computation of Oscillating Airfoil Flows with One- and Two-Equation Turbulence Models, *AIAA Journal*, **32**, 2359-2365.

[36] **Dindar, M. and Kaynak, U.**, 1994. Effect of Turbulence Modeling on Dynamic Stall Computations, AGARD CP-552.

[37] **Ekaterinaris, J.A., Chandrasekhara, M.S. and Platzer, M.F.**, 1995. Analysis of Low Reynolds Number Airfoil Flows, *Journal of Aircraft*, **32**, 625-630.

[38] **Ekaterinaris, J.A., Srinivasan, G.R. and McCroskey, W.J.**, 1994. Present Capabilities of Predicting Two-Dimensional Dynamic Stall, AGARD Cp-552.

[39] **Ekaterinaris, J.A.**, 1995. Numerical Investigation of Dynamic Stall of an Oscillating Wing, *AIAA Journal*, **33**, 1803-1808.

[40] **Akbari, M.H.**, 1999. Bluff-Body Flow Simulations Using Vortex Methods, *PhD Thesis*, McGill University, Montreal, Canada.

[41] **Carr, L.W.**, 1988. Progress in Analysis and Prediction of Dynamic Stall, *Journal of Aircraft*, **25**, 6-17.

[42] **Sankar, N.L. and Tassa, Y.**, 1980. Reynolds Number and Compressibility Effects on Dynamic Stall of a NACA 0012 airfoil, AIAA Paper 80-0010.

[43] **McCroskey, W.J.**, 1982. Unsteady Airfoils, *Ann. Rev. Fluid. Mech.*, **14**, 285-311.

[44] **McCroskey, W.J. and Pucci, S.L.**, 1982. Viscous-Inviscid Interaction on Oscillating Airfoils in Subsonic Flow, *AIAA Journal*, **20**, 167-174.

[45] **Tannehill, J.C., Anderson, D.A. and Pletcher, R.H.**, 1997. Computational Fluid Mechanics and Heat Transfer, Taylor & Francis, Philadelphia.

[46] **CFD-FASTRAN Theory Manual Version 2003,** 2003. CFD Research Corporation, Hunsville, AL, USA.

[47] **Blazek, J.,** 2001. Computational Fluid Dynamics: Principles and Applications, Elsevier Science Ltd., Oxford, UK.

BIOGRAPHY

Erkan Evcan was born on August 24, 1978 in Antalya, Turkey. He completed his high school education in Antalya High School. He attended to Istanbul Technical University to pursue a Bachelor Science Degree in Aeronautical Engineering Department. Then, he attended to Aerospace Engineering Graduate Program in 2002. He worked as a research assistant between December 2002 – January 2005. He is working as a Powerplant Engineer in Turkish Airlines Maintenance Center since January 2005.